Kinematic and Thermodynamic Characteristics of the Flow over the Western Pacific Warm Pool during TOGA COARE

XIN LIN AND RICHARD H. JOHNSON

Department of Atmospheric Science, Colorado State University, Fort Collins, Colorado

(Manuscript received 29 March 1995, in final form 6 September 1995)

ABSTRACT

Rawinsonde and satellite infrared radiation (IR) data from the Tropical Ocean Global Atmosphere (TOGA) Coupled Ocean Atmosphere Response Experiment (COARE) are used to investigate mean and transient behavior and horizontal variability of the atmosphere over the western Pacific warm pool. Infrared data for the 4-mo Intensive Observing Period (IOP) and vertical motion fields indicate that the intensity of convection, height of maximum upward motion, and SST all increased from west (140°E) to east across the COARE domain. IOP-mean IR data show a double ITCZ (Intertropical Convergence Zone) structure north and south of the Intensive Flux Array (IFA, centered at 2°S, 156°E), although marked variability in the patterns occurred on a month to month basis.

Three prominent westerly wind bursts occurred over the IFA during the 4-mo IOP in association with the intraseasonal oscillations (ISOs). Strong upward motion usually occurred 1–3 weeks prior to the peak low-level westerlies. Subsidence dominated when the westerly winds prevailed. COARE data reveal that the vertical wind shear (more than 50 m s^{-1} from 850 to 100 hPa) and the vertical extent of westerlies during the peak westerly wind bursts were far greater than previously recognized. The mean low-level equatorial flow over the western Pacific was westerly, interrupted occasionally by brief periods of easterly flow. The perturbation westerlies to the west of the disturbance associated with the ISO were usually stronger than the perturbation winds to the east. Maximum surface latent heat flux usually occurred during the peak westerlies, whereas the surface sensible heat flux peaked prior to the strongest westerlies.

The IOP-mean divergence profile over the IFA shows a very weak divergence near the surface and weak convergence at middle and low levels. The ITCZ-band divergence profiles show strong low-level convergence from the surface to about 700 hPa. The striking difference between the divergence profiles along the equator over the IFA and those north and south in the ITCZ bands suggests that, although the divergence and vertical motion profiles tend to look alike whenever and wherever the convection is strong, great care should be exercised in generalizing divergence and vertical motion profiles from one region to another over the western Pacific warm pool.

Correlations between cold clouds and vertical motion indicate that cold clouds are a good indicator of upper-level upward vertical motion but not low-level vertical motion. In a significant number of cases, low-level downward motion occurred under very cold cloud tops over the warm pool, indicating extensive optically thick anvil cloud and nonprecipitating high cirrus are a common occurrence over the warm pool.

The IOP-mean relative humidity profile over the IFA shows a primary peak at low levels at the top of the mixed layer and a secondary peak near 550 hPa (near the 0°C level). The secondary peak is not present in either ECMWF or NMC operational analyses, and the midtroposphere is much drier in the two model-assimilated results.

A synthesis of the kinematic and thermodynamic characteristics of the December–early January westerly wind burst as it passed the IFA is presented.

1. Introduction

Tropical convection, especially over the western Pacific warm pool, plays a significant role in global redistribution of heat, moisture, and momentum. This region is not only characterized by the warmest SST in the open oceans but also by the largest annual rainfall and latent heat release in the atmosphere (Webster and Lukas 1992), implying a strong coupling between the ocean and atmosphere. Latent heat released by condensation of water vapor in the tropical atmosphere and surface heat fluxes from the tropical ocean have been considered to act as major heat sources for the global circulation (e.g., Riehl 1954; Riehl and Malkus 1958; Emanuel et al. 1994).

Among the broad temporal and spatial scales of tropical oscillation, the most prominent large-scale feature is the 30–60 day eastward propagating oscillation (hereafter referred to as the intraseasonal oscillation, or ISO), which was first detected by Madden and Julian

Corresponding author address: Mr. Xin Lin, Department of Atmospheric Science, Colorado State University, Fort Collins, CO 80523.
E-mail: lin@swirl.atmos.colostate.edu.

(1971) in the zonal wind and surface pressure in the tropical Pacific. While this oscillation is evident in circulation fields throughout the Tropics (Madden and Julian 1972; Knutson and Weickmann 1987), its signature in convection is generally limited to the eastern Indian and western Pacific Oceans (Madden and Julian 1972, 1994). Strong low-level westerlies usually appear near the equator following the convectively active phase of this oscillation (e.g., Lau et al. 1989; Sui and Lau 1992; Madden and Julian 1994). These anomalous winds, referred to as westerly wind bursts (Luther et al. 1983; Nitta and Motoki 1987), can last from a few days to several weeks. In the past few years, twin tropical cyclones over the tropical western Pacific have received increased attention due to their possible connection with westerly wind bursts (Keen 1988; Ogura and Chin 1987; Nitta 1989; Lander 1990).

Not all westerly wind bursts are associated with the ISO. There is, however, evidence to suggest that the ISO modulates both the frequency and amplitude of higher-frequency convection and westerly burst events (Lau et al. 1989; Gutzler 1991; Sui and Lau 1992; Hendon and Liebmann 1994). Kiladis et al. (1994) have studied convection in the Tropical Ocean Global Atmosphere (TOGA) Coupled Ocean Atmosphere Response Experiment (COARE) region and found that there are prominent oscillations on the 6- to 30-day timescale in conjunction with low-level equatorial westerly wind anomalies, paired anomalous cyclonic circulations straddling the equator, and a strengthening of the sea level pressure gradient along the equator. They also find that the higher-frequency oscillations are often barotropic (westerlies throughout the troposphere), whereas the lower-frequency ISO is typically baroclinic (low-level westerlies surmounted by easterlies).

In recent years, the ISO and westerly wind bursts in the tropical Pacific have received renewed interest since they may serve as triggering mechanisms for the El Niño/Southern Oscillation, which can affect both interannual and intra-annual variabilities of the global climate system (Harrison and Schopf 1984; Lau and Chan 1986, 1988). Connections have also been noted with the Indian and East Asian monsoons (Yasunari 1979; Chang and Lau 1980, 1982; Krishnamurti and Subrahmanyam 1982; Lau et al. 1983), the Australian monsoon (Holland 1986; Hendon and Liebmann 1990a,b), tropical storms (Gray 1979), and weather patterns in middle latitudes (e.g., Lau and Chan 1986; Magaña and Yanai 1991). Nakazawa (1988), using Geostationary Meteorological Satellite (GMS) IR data, showed that the ISO in the tropical western Pacific is associated with one or more eastward-moving super cloud clusters, with successive formation of new individual cloud clusters east of the mature stage cloud clusters. Individual cloud clusters embedded within super cloud clusters move westward.

Several theories have been proposed to explain the origin and characteristics of the ISO: wave–CISK (e.g., Chang 1977; Lau and Peng 1987; Chang and Lim 1988; Wang 1988), forcing response (e.g., Yamagata and Hayashi 1984; Hu and Randall 1994), and wind-induced surface heat exchange (WISHE) (Emanuel 1987; Neelin et al. 1987; Yano and Emanuel 1991) (see the review by Hayashi and Golder 1993). However, most of these ideas have not been tested or proven by observations, and many remain unexplained due to insufficient surface and upper-air records over the tropical western Pacific, particularly over open oceans. Outgoing longwave radiation (OLR) data are not able to provide the basic kinematic and thermodynamic features, which are essential to understanding the dynamics of the ISO. Its relationship with surface rainfall rates and vertical heating profiles is still not well understood. Model output analyses, although they can provide high temporal and spatial resolution datasets, are sensitive to different physical parameterization schemes (e.g., Emanuel 1988; Chao and Lin 1994) and assimilation constraints.

The November 1992–February 1993 TOGA COARE (Webster and Lukas 1992) was designed to improve understanding of the role of the western Pacific warm pool in the mean and transient state of the tropical ocean/atmosphere system. Various meteorological and oceanographic observations were taken in order to describe and understand the principal processes responsible for the coupling of the ocean and the atmosphere in the warm pool system. Several westerly wind bursts occurred over the TOGA COARE domain during the 4-mo intensive observing period (IOP), providing a unique opportunity to investigate the mean and transient behavior and horizontal variability of the atmosphere over the warm pool.

OLR data and NMC (National Meteorological Center, now National Centers for Environmental Prediction) divergent wind fields presented in Gutzler et al. (1994) indicate the climatological mean center of deep convection during the COARE IOP was located near and just west of 180°. Their analyses show that a large envelope of deep convection typically developed over the Indian Ocean, then propagated eastward into the TOGA COARE large-scale array (LSA), intensified somewhat over the warm pool, and finally dissipated after passing the date line, probably due to the cooler sea surface. Velden and Young (1994), using satellite observations, noticed a marked increase in disorganized, quasi-stationary cloudiness/convection over the warm pool during the active phase of the ISO. A rich variety of higher-frequency fluctuations existed, in addition to prominent intraseasonal oscillations.

Given that the western Pacific warm pool is a focal point for deep convection as well as the highest amplitude of tropical intraseasonal variability, including westerly wind bursts, it is important to document the basic kinematic and thermodynamic features of the at-

mosphere and its convective variability over the period of TOGA COARE. In this study, all available rawinsonde and satellite IR data collected from the 4-mo COARE IOP are analyzed in detail to investigate the mean and transient state and horizontal variability of the atmosphere over the western Pacific warm pool. Large-scale circulation features over the LSA, as well as mesoscale features within the intensive flux array (IFA), will be documented. Emphasis will be placed on the temporal and spatial evolution relating to the westerly wind bursts. Section 2 will describe data and analysis methods used in this study. Section 3 will document the mean IR distribution. Section 4 will give the basic structure of kinematic features. Section 5 will discuss the basic thermodynamic features. A synthesis of observations of the large-scale westerly wind burst is presented in section 6. Section 7 will contain a summary and some concluding remarks.

2. Data and analysis methods

a. Data

Figure 1 shows the TOGA COARE sounding network, which was established over the equatorial western Pacific to determine the mesoscale to synoptic-scale structure of atmospheric circulation systems over the warm pool. It consisted of nested arrays, ranging from the synoptic scale (the LSA, 10°S–10°N, 140°E–180°, with twice per day soundings) to the subsynoptic and mesoscales (the outer sounding array, or OSA, and the IFA, both with four per day soundings). The IFA was centered at 2°S, 156°E bounded by a polygon consisting of two land stations, Kapingamarangi (1°N, 154°E) and Kavieng (3°S, 151°E), and two research vessels, the *Kexue #1* (4°S, 156°E) and the *Shiyan #3* (2°S, 158°E). The majority of the high-density meteorological and oceanographic observations in COARE were taken within the IFA. Integrated sounding systems (ISS, Parsons et al. 1994), consisting of Omegasondes, 915-MHz wind profilers, acoustic sounders, and surface meteorology stations, were employed at these four sites. Soundings were also released from research vessels including *Xiangyanghong #5, Vickers,* and *Moana Wave* within the IFA.

All available sounding data from the stations in Fig. 1 were combined to perform computations at 6-h intervals throughout the 4-mo IOP from 1 November 1992 to 28 February 1993. Table 1 shows the number of released soundings and instrument type for stations within the OSA that were used in this study during the COARE IOP. In this paper we will concentrate on describing the basic kinematic and thermodynamic features over the IFA relating to the three westerly wind bursts, and monthly and IOP mean structure over the IFA and LSA.

During the TOGA COARE IOP, the Vaisala humidity sensor mounted on the Omegasonde was used to detect the water vapor over the OSA and IFA. It provides accurate and high-resolution humidity data in the lower and middle troposphere. Unfortunately, mea-

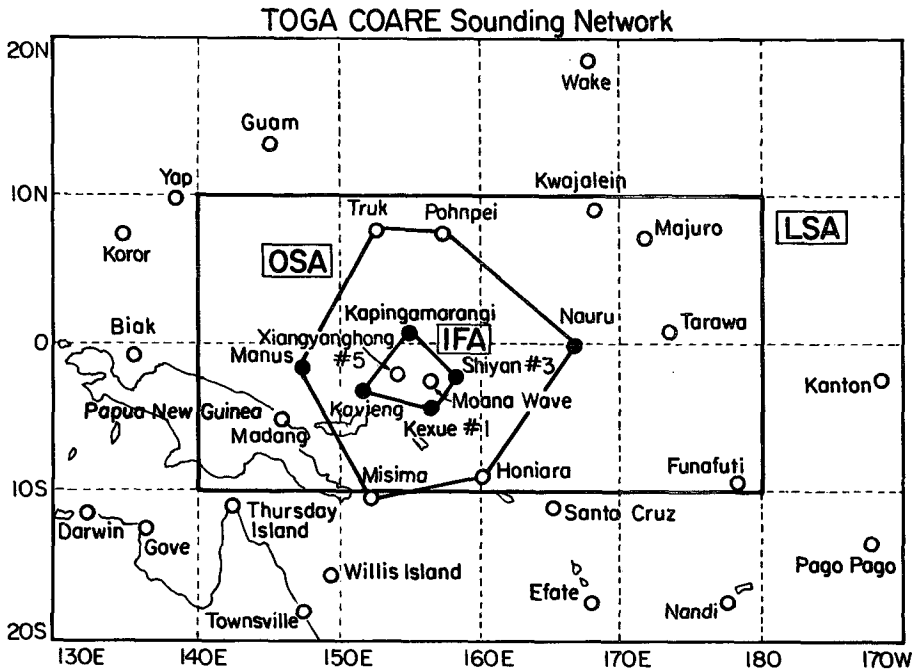

FIG. 1. The TOGA COARE sounding network. The solid circles indicate ISS stations, and the open circles represent other sounding stations.

TABLE 1. Some characteristics of sounding stations within Large Scale Array during COARE IOP.

Station name	Number of soundings	Instrument type	Station type
Truk	477	Omega	Island
Honiara	414	ISS	Island
Kapingamarangi	475	ISS	Atoll
Kavieng	468	ISS	Island
Kexue #1	356	ISS	Ship
Manus	448	ISS	Island
Moana Wave	257	Omega	Ship
Nauru	471	ISS	Island
Pohnpei	480	Omega	Island
Shiyan #3	330	ISS	Ship
Vickers	111	Omega	Ship
Xiangyanghong #5	263	Omega	Ship

surements from the field showed the sensor to regularly "ice up" at temperatures below about −44°C (about 250 hPa) so that the upper-level humidity could not be sampled. However, this problem does not affect the main results of our study.

Japanese GMS brightness temperature data (courtesy of Dr. T. Nakazawa) were used to facilitate the analysis. The data, collected every hour, have a spatial resolution of approximately 11 km. Data for each pixel were first averaged to get values in a 1° grid box, and then the box values were averaged to generate mean brightness temperatures over the LSA and the IFA-mean time series. Some European Centre for Medium-Range Weather Forecasts (ECMWF) and NMC model-assimilated analyses obtained from the National Center for Atmospheric Research (NCAR) were also used.

The improved meteorological surface mooring (IMET, data courtesy of R. Weller and S. Anderson), operated by the Woods Hole Oceanographic Institution (WHOI), was employed at the center of the IFA (1°45′S, 156°E). The meteorological and oceanographic packages mounted on it provided information, including surface wind, relative humidity (RH), barometric pressure, SST, and air temperature at a 1-min rate. Surface latent and sensible heat fluxes were calculated according to bulk aerodynamic formulation developed by Liu et al. (1979) and subsequently revised (Version 1.0) for COARE by Fairall et al. (1995). In order to compare with the COARE sounding analyses, daily mean surface heat fluxes, surface wind speeds, and SSTs were obtained by averaging hourly data centered at 0000, 0600, 1200, and 1800 UTC.

b. Analysis methods

ISS Omegasondes provided high quality information on pressure, temperature, dewpoint temperature, zonal and meridional wind components, and latitude and longitude of the measurement at approximately 50-m vertical resolution. Quality control parameters for pressure, temperature, relative humidity, and zonal and meridional wind components were utilized to exclude bad data from the analyses (e.g., unreliable surface humidity values from several of the ISS sites). Additional hydrostatic, horizontal, and statistical checks were performed to eliminate erroneous sounding data.

The rawinsonde data (temperature, specific humidity, zonal and meridional wind components, and height) were first vertically interpolated from 1000 to 25 hPa at intervals of 25 hPa. A 1–2–1 smoothing scheme was used to filter out small-scale fluctuations in the vertical. Then, the data were objectively interpolated onto a 1.0° by 1.0° grid over a region larger than the LSA (130°E–170°W, 20°S–20°N) using several different approaches described below.

In previous studies involving tropical field experiments over the western Pacific and the eastern Atlantic, several different analysis techniques have been used to determine horizontal divergence, for example, the Bellamy (1949) or line-integral method, the least squares fitting, and the optimal statistical interpolation (Ooyama 1987). The line-integral method is usually used over small areas surrounded by three or more stations. The area-averaged properties can be coarsely estimated, although problems can occur with poor distribution of the stations and nonlinear variations of fields between vertices (Davies-Jones 1993). The least squares fitting method usually utilizes a linear or quadratic surface to approximately represent the horizontal fields. It is suitable for an analysis over a small area where the curvature of the surface is small. However, for the areas considered and the uneven distribution of COARE stations, including the existence of several sounding sites within the IFA, it is found that neither a linear surface nor a quadratic surface is accurate enough to represent the variations of basic fields over the IFA and OSA, especially for moisture and wind fields. The Barnes analysis scheme (Barnes 1964, 1973) has been used in this study. The percentage of the resolved wavelengths can be easily estimated by varying the influence radius. Large-scale and mesoscale features can be recovered, while smaller-scale disturbances are suppressed. A cubic-spline analysis package (courtesy of Dr. S. Lord at NMC), which is based on the mechanical interpolation method described by Ooyama (1987), was also tested. The results were very similar to those from the Barnes analysis.

Since the average distances between sounding stations within the COARE domain varied considerably from about 300 km in the IFA to 700 km in the OSA, values at each grid point were interpolated from the six closest stations. A filter response of about 50% at the mean distance among the grid point and the six stations was selected. Soundings were generally released twice per day outside of the OSA. In this study, unless otherwise specified, the IFA-averaged profiles are based on data at 6-h intervals, while horizontal and vertical cross sections over larger areas are based on data at 0000 and

1200 UTC. Spatial derivatives were calculated using a finite centered difference method. Vertical velocities were calculated by integrating the mass continuity equation in p coordinates from the surface to the tropopause. A constant correction has been applied at each grid point to the divergence at all levels to satisfy mass continuity for the whole volume. Vertical velocity at 75 hPa was set to zero since the tropopause was usually between 100 and 85 hPa in the tropical western Pacific. Vertical velocity at the surface was computed from surface wind and pressure data.

3. Mean IR distribution

To define the mean location of deep convection over the warm pool and study its seasonal transition, the IOP-mean brightness temperature over the LSA and monthly averaged distributions are shown in Fig. 2. The IOP-mean brightness temperature (Fig. 2a) indicates that the maximum deep convection was east of the IFA. The IFA was in a transition zone with a minimum in deep convection to the west. A double-ITCZ structure can be observed: the northern one was located between 2° and 5°N, while the Southern Pacific convergence zone (SPCZ) was close to the equator around 170°E and extended southeastward across the date line. Cold clouds were usually found over large islands such as New Guinea.

In November (Fig. 2b), two cold cloud bands can be observed in the eastern part of the LSA with their lowest values located at 7°N and 7°S, respectively. Over the IFA region there was a large zonal gradient along the equator with convection being generally suppressed over the western part of the LSA. A large single cold cloud band can be observed in the December mean plot (Fig. 2c) south of the equator, extending from 140°E to the date line. This convection was associated with the December westerly wind burst. In January (Fig. 2d), there was a cold cloud band (between 2° and 7°N) in the Northern Hemisphere extending across the LSA with the strongest convection in the east. Convection in the Southern Hemisphere and SPCZ was notably weak in January. The February mean plot (Fig. 2e) indicates a quite different pattern from previous months. The area covered by cold clouds increased dramatically, and most cold clouds were over the central and eastern LSA. The double-ITCZ structure became quite clear across the LSA. To summarize, although there was a general north to south shift in convection during the IOP, marked variability in the patterns occurred on a month to month basis.

4. Basic kinematic features

a. Zonal wind

Climatological studies show that weak easterly winds generally dominate the low levels along the equator in the tropical western Pacific with speeds on

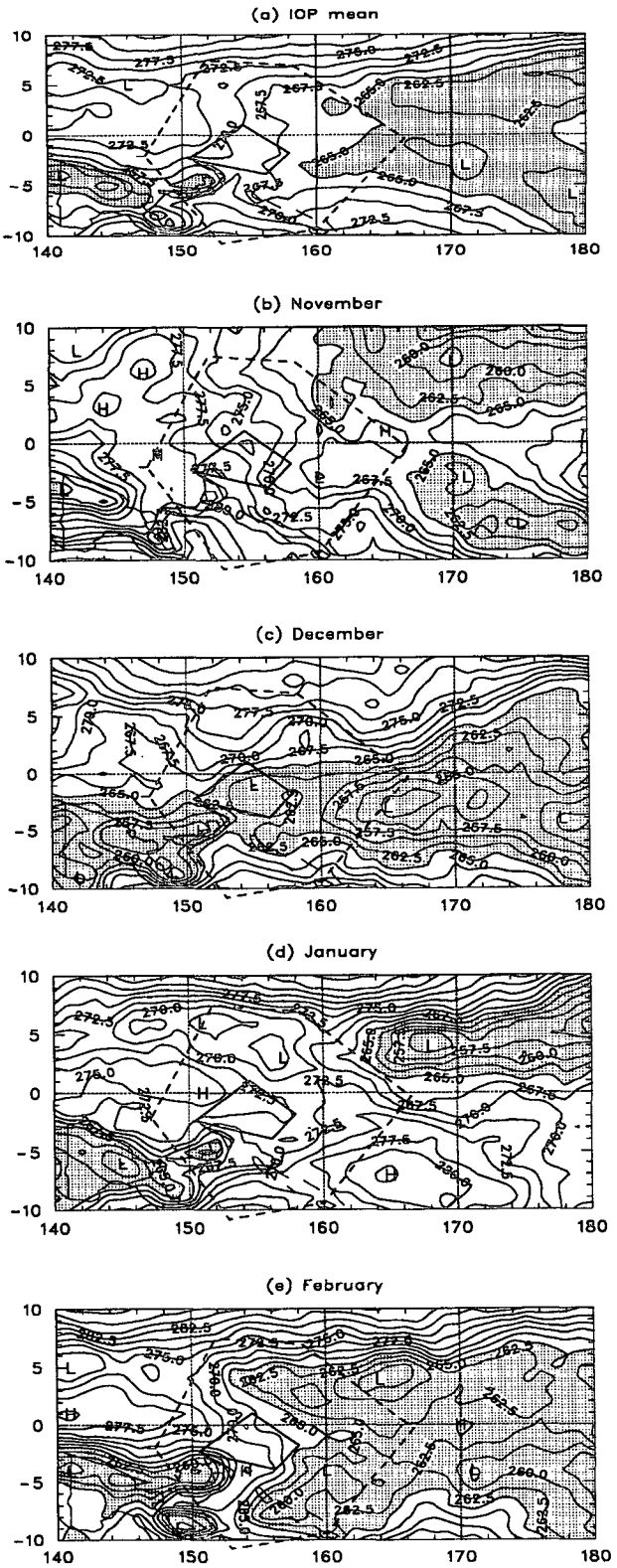

FIG. 2. IOP-mean and monthly mean brightness temperatures over the Large Scale Array. Contour intervals 2.5 K, and areas with temperature less than 265 K are shaded. (a) IOP mean, (b) Nov, (c) Dec, (d) Jan, (e) Feb.

the order of 1–5 m s^{-1} (Lau 1985; Peixoto and Oort 1992). The easterlies are often interrupted by westerly wind bursts on intraseasonal timescales in association with the Madden–Julian Oscillation (Madden and Julian 1971, 1972) or extratropical interactions, for example, via cold surges (Love 1985; Chu 1988; Kiladis et al. 1994). Figure 3a shows the time series of the zonal wind component averaged over the IFA at 0000 UTC throughout the IOP (5-day running mean). Three prominent westerly wind burst periods can be clearly identified during the 4-mo IOP: 1) early to mid-November, 2) middle December to early January, and 3) late January to the end of February. The December–January case was a major event (Gutzler et al. 1994; Velden and Young 1994): the westerly winds first developed near the surface from 10 to 15 December and gradually increased in depth and magnitude. Maximum westerly winds occurred around 1 January between 850 and 600 hPa at speeds exceeding 12 m s^{-1}, while maximum easterlies in excess of 32 m s^{-1} were found at about 100 hPa. Unfiltered zonal wind shows maximum easterlies of 37 m s^{-1} in the upper troposphere and maximum westerlies of 17 m s^{-1} at low levels. The westerly winds at this stage dominated most of the troposphere and extended from the surface up to 200 hPa. The great vertical extent of the westerlies in this case may have been influenced by Tropical Cyclones Kina and Nina to the south of the IFA. The strong vertical wind shear and out-of-phase relationship between upper- and lower-level winds are consistent with previous findings (Madden and Julian 1971, 1972; Knutson and Weickmann 1987). The westerlies stopped abruptly and reversed to easterlies in the middle and lower troposphere toward mid-January, while strong westerlies appeared in the upper troposphere. Between 50 and 150 hPa, there appears to be some evidence of downward propagating equatorial Kelvin waves (Wallace and Kousky 1968; Gutzler et al. 1994) from 1 December through the end of February. Above 50 hPa in the stratosphere, the zonal wind field was in general dominated by westerlies since the IOP was during the westerly phase of the quasi-biennial oscillation (QBO). The gradual downward propagation of the QBO westerly regime is also readily apparent in Fig. 3a.

Figure 3b shows the IOP-mean zonal wind profile over the IFA based on 6-h data. To illustrate the dramatic change in the vertical wind shear during the westerly wind burst, daily averaged vertical profiles for 11 December and 1 January are shown. In the mean, there were westerlies at low levels, and easterlies aloft. The 11 December profile was at a time of strong upward motion (Fig. 9, later) and deep convection as westerlies converged with easterlies at low levels near the IFA. Weak westerlies existed from the surface to 900 hPa, and easterlies above. Vertical wind shear in the mid-troposphere was relatively weak. On 1 January, when the convection was suppressed over the IFA (Fig. 9, later), westerly winds in the lower troposphere reached a maximum (about 17 m s^{-1}), with easterlies at nearly 35 m s^{-1} at 100 hPa. This vertical wind shear of over 50 m s^{-1} through the depth of the troposphere was probably too strong to support deep convection, as found in some midlatitude studies (e.g., Weisman et al. 1988). The vertical wind shear and the vertical extent of westerlies during the peak westerly wind bursts were far greater than previously recognized.

In order to examine the evolution of the meridional structure of the westerly wind bursts near the surface, a time–latitude cross section of zonal component of the wind at 1000 hPa was constructed using gridded data between 150° and 160°E, where the sounding station network during the IOP was dense. Again, three westerly wind bursts can be identified during the 4-mo period (Fig. 4a). In the November case, the westerlies first developed between 4°N and 10°S, with a peak at 2°N. Then they migrated northward between 10 and 25 November, with the maximum located between 3° and 10°N around the time of the development of Typhoons Gay and Hunt in the northwest Pacific. Both the December–January and the February cases occurred south of 3°N, with their westerly maxima originating near the equator and then shifting to around 5°S over a ~1-week period. This southward shift is related to the development of tropical cyclones in the Southern Hemisphere following the westerly wind bursts (e.g., Keen 1982; Nitta 1989; Lander 1990; McBride et al. 1995). In the December case, Tropical Cyclones Kina and Nina formed in the southwest Pacific, whereas in February it was Tropical Cyclone Oliver. Easterly trade winds dominated to the north of 3°N from December to February.

During the TOGA COARE IOP, deep convection and maximum precipitation associated with the ISOs usually occurred 1–3 weeks prior to the peak westerly wind bursts. The behavior can be seen particularly well for the December burst by comparing IR data (Fig. 4b) with 1000-hPa zonal winds (Fig. 4a). It is interesting to note that low-level westerly winds following the IR minimum were always stronger than the winds preceding it, similar to the flow pattern derived from an analytic model for heat-induced tropical circulation (Gill 1980). The absence of significant easterly flow can be seen alternatively (to avoid the possible bias of very strong surface westerly winds in a few cases) in a frequency distribution of the 1000-hPa zonal wind component in 1 m s^{-1} bins over the IFA at 6-h intervals during COARE IOP (Fig. 4c). It is evident that there was a general absence of strong equatorial easterlies over the IFA and that the mean zonal flow was westerly during the three ISO events (although the easterlies were slightly undersampled because the easterly phase of the first ISO occurred before 1 November). This evidence does not appear to support the WISHE mechanism (Emanuel 1987; Neelin et al. 1987), which requires a preexisting tropical mean easterly flow and stronger perturbation winds to the east of the distur-

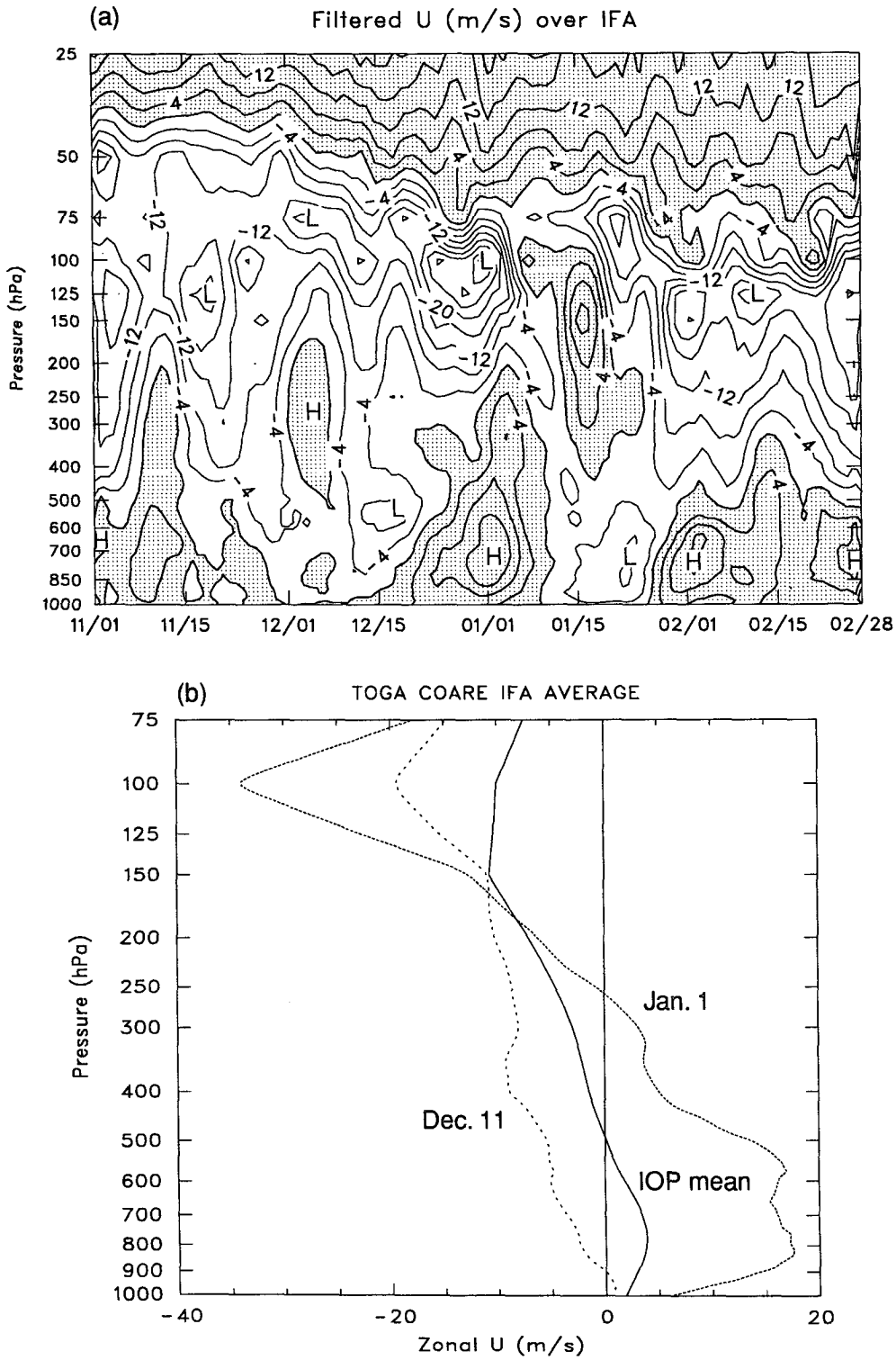

FIG. 3. (a) Time series of zonal U component (m s^{-1}) at 0000 UTC averaged over the Intensive Flux Array (5-day running mean). Contour intervals 4 m s^{-1}, and westerlies are shaded. (b) The IOP-mean vertical profile of zonal U component over the IFA (solid curve), and daily averaged U profiles on 11 Dec and 1 Jan. Positive values indicate westerlies.

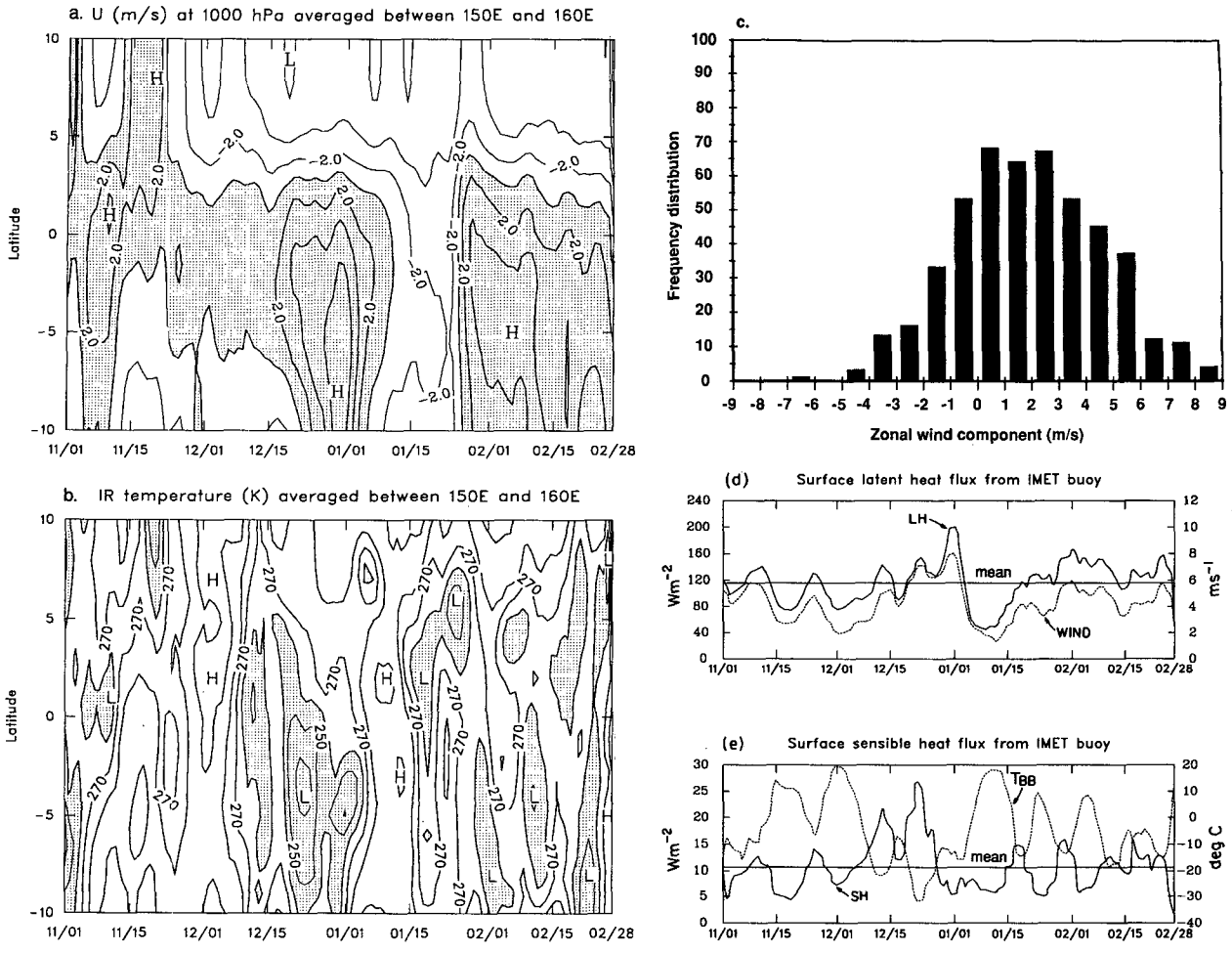

FIG. 4. (a) Time–latitude cross section of zonal component of the wind at 1000 hPa. Westerlies are shaded. The intervals are 2 m s^{-1}. (b) Time–latitude cross section of GMS brightness temperature (in K). The regions with T less than 260 K are shaded. (c) Frequency distribution of zonal wind component at 1000 hPa over the IFA during COARE IOP. Ordinate values are numbers of 1000-hPa zonal wind component during the COARE IOP at 6-h intervals. Positive values indicate westerlies. (d) Time series of the surface latent heat flux (solid line) from WHOI IMET buoy (W m^{-2}). Superimposed is surface wind speed (dashed line) from the IMET buoy (m s^{-1}). Mean latent heat flux of 117 W m^{-2} is indicated. (e) Time series of the surface sensible heat flux (solid line) from WHOI IMET buoy (W m^{-2}). Superimposed is GMS brightness temperature (dashed line) over the IFA. Mean sensible heat flux is indicated. (The IMET buoy data courtesy of R. Weller and S. Anderson, WHOI).

bance to explain the maintenance and eastward propagation of the 30–60 day oscillation. An easterly acceleration of the flow did occur north of 5°N around 1 December (about 2 weeks prior to the heaviest rainfall); however, it was weak, and analyses similar to Fig. 4a between 160° and 170°E and between 170° and 180° (not shown) indicate no concurrent easterly acceleration east or northeast of the IFA.

Further evidence that enhanced evaporation follows rather than leads ISO convection can be seen in time series of surface latent and sensible heat fluxes from the IMET buoy (Figs. 4d and 4e). The surface latent heat flux (Fig. 4d) exhibited a good correlation with surface wind speed. During the late-December and late-January westerly wind bursts, evaporation began increasing 3–4 weeks prior to the peak westerlies. Pronounced increase of the latent heat flux also occurred when disturbances passed, probably induced by convective and mesoscale downdrafts. Evaporation reached its maximum during the peak westerly wind bursts when maximum deep convection had moved to the east of the IFA (not shown). The surface sensible heat flux (Fig. 4e) shows a different pattern from that of the latent heat flux. It correlates better (in a negative sense) with the brightness temperature than with the surface wind speed, presumably as a result of strong winds and cool downdrafts associated with deep convection and heavy precipitation. In summary, time series of evaporation and sensible heat flux at the IMET buoy indicates that maximum surface energy transfer

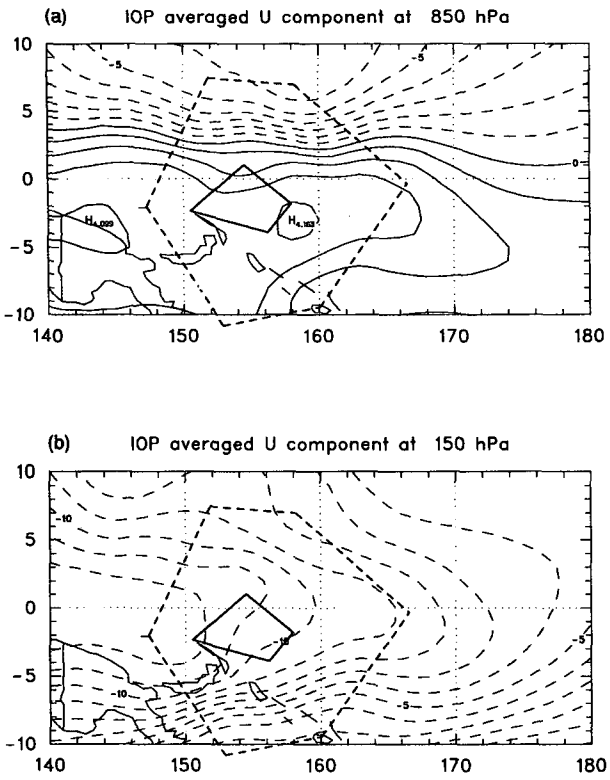

FIG. 5. The IOP-mean zonal wind component at (a) 850 and (b) 150 hPa over the Large Scale Array. Solid lines indicate westerlies, while dashed lines represent easterlies. The intervals are 1 m s^{-1}.

usually occurred during and after the arrival of the convectively active phase of the 30–60 day oscillation, not before.

The IOP-averaged zonal wind components at 850 and 150 hPa over the LSA are illustrated in Fig. 5. During the IOP, the wind pattern at 850 hPa was very similar to that at 1000 hPa, although both westerlies and easterlies were stronger at 850 hPa. Westerly winds generally dominated the warm pool between 3°N and 10°S, with maxima located at about 3°S. The westerlies were stronger west of 165°E and decreased toward the date line, consistent with the observations of an IR minimum in the eastern part of the LSA (Fig. 2). There was a strong horizontal shear near 4°N, which separated the northeast trades from the equatorial westerlies. At 150 hPa (Fig. 5b), the mean zonal wind was everywhere easterly. The maximum easterlies were located at the equator in the western part of LSA, again consistent with maximum convection toward the east.

b. Meridional wind

In their review paper, Madden and Julian (1994) summarized some results of the 30–60 day oscillation in the Tropics and found little evidence that the meridional wind played a role in the variations within individual seasons (Madden and Julian 1971; Parker 1973). Figure 6a shows the time series of the IFA-mean vertical profiles of the meridional wind component. Although the signal was much weaker than that in the zonal wind profiles, northerly winds usually occurred and strengthened at low levels when the westerly wind bursts developed (e.g., 1 January and 1 February cases). The westerly wind burst was actually a west-northwesterly flow over the IFA. Southerly flows can be observed at upper levels during these periods.

Figure 6b contains the IOP-averaged meridional wind component over the IFA, as well as vertical profiles for 11 December and 1 January. Since the IFA was at times located between double-ITCZ bands and other times not (Fig. 2), the IOP-mean meridional wind component was very small and fluctuated with height. On 11 December, when convection was enhanced over the IFA, northerly winds generally domi-

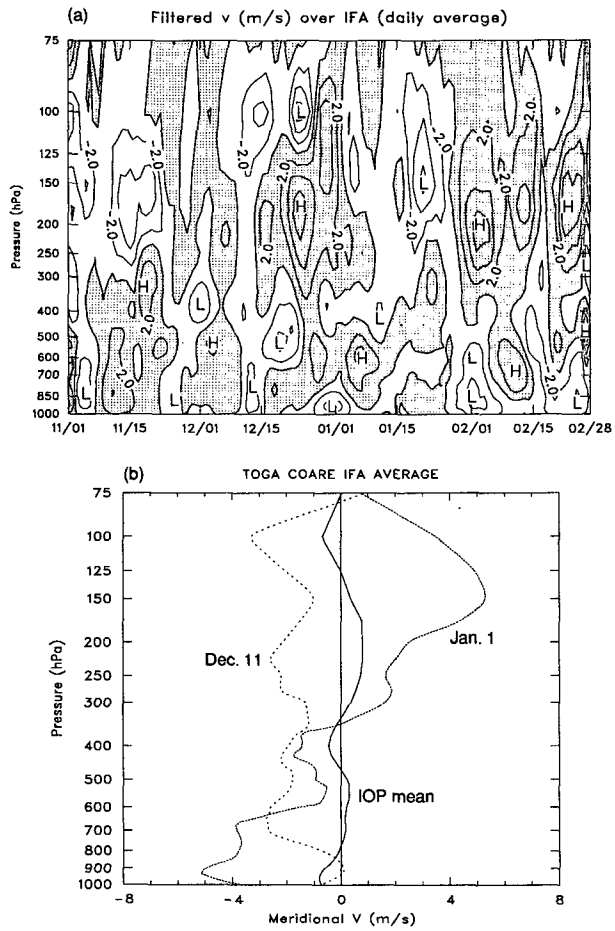

FIG. 6. (a) Time series of daily mean meridional V component (m s^{-1}) averaged over the Intensive Flux Array (5-day running mean). Contour intervals are 2 m s^{-1}, and southerlies are shaded. (b) Vertical profiles of meridional wind (in m s^{-1}) averaged over the IFA. The solid line represents the IOP mean, and dashed lines are for 11 Dec and 1 Jan cases.

nated the entire troposphere with weak vertical wind shear except at levels below 700 hPa. On 1 January, when the low-level westerly wind burst reached its peak, there were relatively strong northerlies over the IFA below 600 hPa with southerlies above with a peak of about 5 m s^{-1} near 150 hPa. This vertical profile of v is consistent with the existence of inflow at low levels and outflow aloft from deep convection and Tropical Cyclones Kina and Nina to the south of the IFA (Fig. 4b).

c. Divergence

Figure 7 illustrates a north–south cross section of IOP-mean divergence averaged between 150° and 160°E. Two convergence maxima are located at low levels between 5°–8°S and 2°–5°N, with corresponding divergence maxima at upper levels. This pattern is consistent with the double-ITCZ structure shown in Fig. 2a at the longitudes of the IFA.

The IFA was located between the double-ITCZ bands, at least in an IOP-mean sense. The divergence pattern over the IFA was quite different from that within the ITCZ bands to the north and south (Fig. 8). Over the IFA, weak convergence occurred at middle and low levels with divergence in the upper troposphere. Maximum convergence was located between 700 and 800 hPa with very weak divergence near the surface. On the other hand, the profiles in the ITCZ bands show strong low-level convergence from the surface to about 700 hPa with strong divergence aloft. These profiles are more consistent with those from previous studies of the tropical western Pacific (Reed and Recker 1971; Yanai et al. 1973). Yanai et al. (1973) investigated the basic kinematic features within the ITCZ using sounding data from the Marshall Island region (centered near 8°N). Their divergence profile shows a deep layer of convergence from the surface to 350 hPa with a peak located at 950 hPa and divergence aloft peaking near 200 hPa. Their findings are very similar to the profiles at 4°N and 7°S during COARE IOP, where the mean double-ITCZ bands were located, although the convergence in our case only extended to 475 hPa. During periods of deep convection over the IFA, the divergence profile (not shown) looks like those at 4°N and 7°S, suggesting similar convective characteristics whenever and wherever convection is strong. However, the striking difference between the IOP-mean IFA- and ITCZ-band divergence profiles, particularly at low levels, over short north–south distances suggests that great care should be exercised in generalizing divergence and vertical motion profiles from one region to another over the western Pacific warm pool.

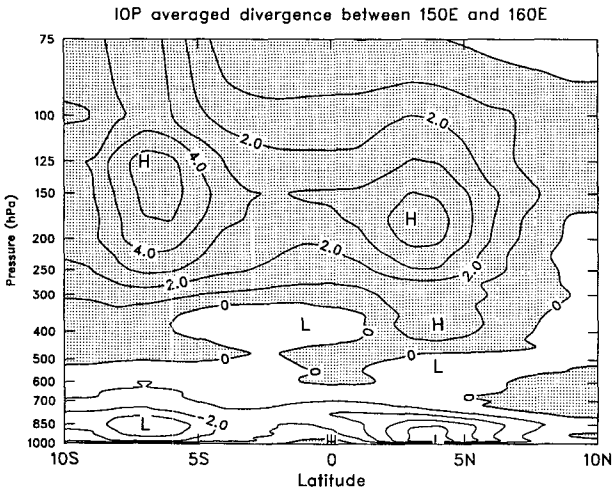

FIG. 7. North–south cross section of horizontal divergence averaged between 150° and 160°E (10^{-6} s^{-1}). Positive regions, indicative of divergence, are shaded.

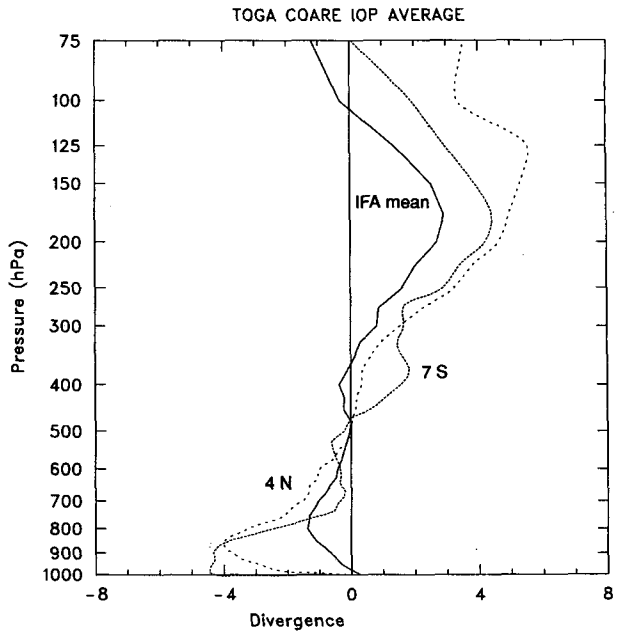

FIG. 8. The IOP-averaged vertical profiles of horizontal divergence over the IFA and the double-ITCZ bands (4°N and 7°S)(10^{-6} s^{-1}).

d. Vertical motion

Time series of brightness temperature from Japanese GMS satellite data, vertical motion over the IFA, and wind speed at 1000 hPa from the COARE analyses are shown in Fig. 9. The sounding-derived vertical motion pattern is, in general, consistent with satellite data: strong upward motion usually corresponds to increased high clouds (lower brightness temperatures), whereas downward motion or weak upward motion usually corresponds to decreased high clouds (higher brightness temperatures). Maximum upward motion implying heavy precipitation usually occurred 1–3 weeks prior

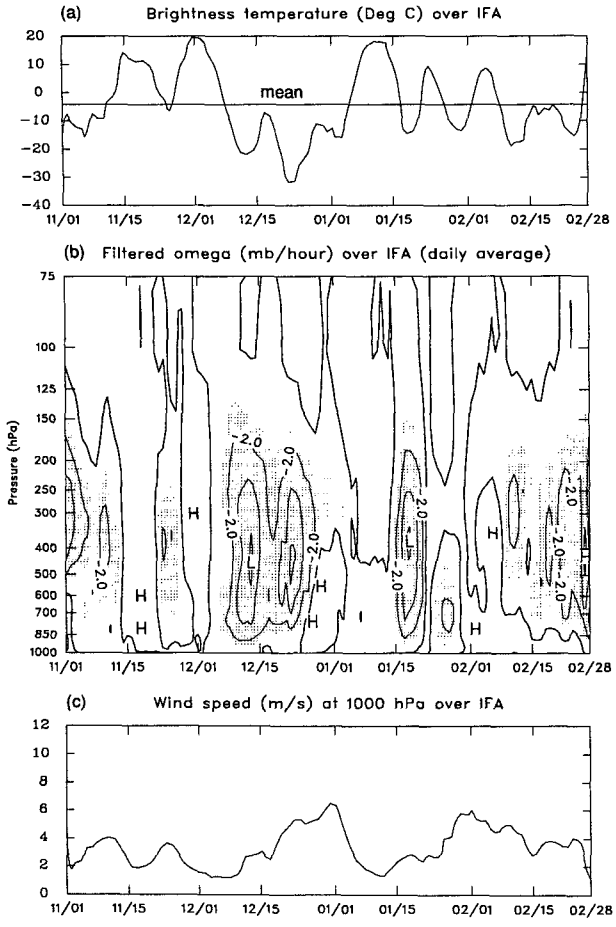

FIG. 9. (a) Time series of the IFA-averaged GMS brightness temperature (°C). (b) Time series of the IFA-averaged vertical motion (mb h^{-1}) throughout the COARE IOP. Areas with $\omega \leq -1.0$ mb h^{-1} are shaded. (c) Time series of 1000-hPa wind speed over the IFA (5-day running mean).

to the peak westerly wind bursts when the surface winds were strongest (e.g., December and January cases), consistent with previous satellite observations of Knutson and Weickmann (1987). The upward motion maxima were usually located at upper levels between 500 and 350 hPa. Low-level subsidence or weak upward motion was observed when strong westerly winds prevailed (also corresponding to times of strong vertical wind shear between 850 hPa and the tropopause, Fig. 3).

Toward 1 January, when the westerly wind burst reached its peak, subsidence generally dominated the middle and low levels over the IFA, but the brightness temperatures remained quite low. Rainfall analyses by Lin and Johnson (1994) based on rawinsonde-derived results and satellite data suggest that the relatively low brightness temperatures over the IFA during this period were a result of the frequent occurrence of nonprecipitating high cirrus. The cirrus advected across the IFA from convection to the east by strong easterly flow (Fig. 3a).

Methods using satellite data have been developed to estimate rainfall rate according to the relationship between cold clouds and deep convection (e.g., Arkin and Meisner 1987). However, it is not clear how well cold clouds correlate with vertical motion at all levels of the atmosphere. Figure 10 shows scatterplots of brightness temperature versus ω at 300 and 700 hPa, respectively, over the IFA using 6-h data. Omega at 300 hPa (Fig. 10a) shows a nearly linear correlation with brightness temperature, suggesting that cold clouds are a good indicator of upper-level vertical motion. For brightness temperatures less than −20°C (253 K, the IFA-averaged temperature at 375 hPa), all but three cases show upward motion at 300 hPa. However, such is not the

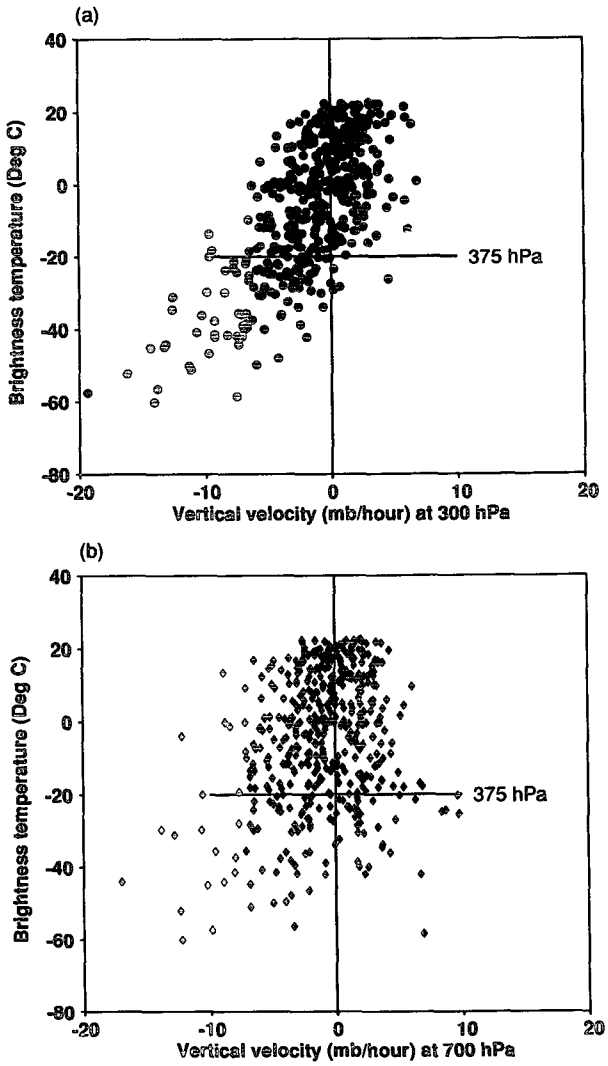

FIG. 10. Scatterplots of brightness temperature and vertical motion over the IFA: (a) ω at 300 hPa, (b) ω at 700 hPa.

case for vertical velocity at 700 hPa (Fig. 10b). For the IFA-averaged cloud tops above 375 hPa, about one-third of the cases indicate downward motion at 700 hPa. Extensive optically thick anvil cloud and nonprecipitating high cirrus dominated the IFA during these periods. Many of these cases occurred in high wind shear regimes, when strong easterlies advected cirrus westward from convection to the east of the IFA. A number of the cases are also probably associated with extensive stratiform precipitation anvils, which characteristically have downward motion in the lower troposphere (Houze 1982). For brightness temperatures above −20°C (cloud top below about 375 hPa), roughly half the cases indicate upward motion and half indicate downward motion. In this situation, vertical motion at 700 hPa is essentially independent of cloud-top temperature.

Figure 11 shows the IOP-mean and monthly mean north–south cross sections of ω averaged between 150° and 160°E. Although there were large monthly variations across the equator, a region of significant upward motion, which corresponds to the ITCZ, can be clearly observed in each hemisphere, consistent with the two convergence/divergence couplets shown in the divergence plot (Fig. 7). The IOP-mean plot (Fig. 11a) indicates that upward motion generally dominated the tropical western Pacific, although weak subsidence can be noticed north of 8°N, probably induced by the subtropical high in the Northern Hemisphere. The SPCZ was stronger than the northern ITCZ during COARE IOP, with peak upward motion around 7°S between 350 and 600 hPa, while the northern ITCZ had its peak ω located near 4°N between 400 and 650 hPa. The order of magnitudes and altitudes of the peak upward motion within the ITCZ bands were quite similar to previous studies over the western Pacific (e.g., Nitta 1972; Yanai et al. 1973). The IFA, which was located between the two significant rising regions, had relatively constant upward motion between 700 and 250 hPa.

Consistent with the IR data (Fig. 2b), convection was generally suppressed in November between 150° and 160°E, and upward motion was weak (Fig. 11b). The peak of the SPCZ was located between 4° and 1°S, which is closer to the equator than the IOP mean. The northern ITCZ had its peak located between 4° and 5°N and extended farther north than in the later months, consistent with a gradual transition of the convergence zone from boreal autumn to boreal winter. Downward motion occurred south of 7°S, presumably due to the control of the Southern Hemisphere subtropical high. Deep convection intensified in December to the south of the equator, and upward motion predominated the tropical southwestern Pacific with the peak upward motion shifting to 7°S (Fig. 11b). The northern ITCZ also intensified, migrating 1° south with its peak located at low levels near 600 hPa. Due to the influence of the strong westerly wind burst in early January, convection was suppressed to the south of the equator during the first few days of the month. The January mean upward motion weakened within the SPCZ (Fig. 11d), with a peak located at low levels between 550 and 750 hPa. On the other hand, the northern ITCZ strengthened and had its peak at higher levels, consistent with satellite data (Fig. 2d). Although the large-scale circulation patterns changed, the position of the double-ITCZ was almost the same as it was in December. In February, vigorous convection started again in both hemispheres (Figs. 2e and 11e), and the SPCZ reached its maximum at about 7°S. Downward motion can be observed near the equator from the surface to 800 hPa, probably induced by strong convergent flows into the double ITCZ.

In order to examine the zonal variations of vertical motion in the tropical western Pacific, an east–west cross section of IOP-mean ω (Fig. 12a) was constructed from 140°E to 180° using gridded data at 0000 UTC and 1200 UTC between 5°N and 5°S. Mean upward motion generally increased toward the east, the strongest values being located around 170°E (acknowledging that caution should be exercised since data east of 170°E are sparse), consistent with the findings in Fig. 2, which showed the lowest IOP-mean brightness temperature over this region. The Gutzler et al. (1994) December–January–February averages of OLR across the LSA also indicate the center of deep convection near the date line. The upward motion was quite weak in the western part of the LSA, and downward motion can be observed around 144°E between 850 and 300 hPa. Although the IOP-mean plot (Fig. 2a) shows that there were considerable cold clouds at 5°S over the land between 140° and 150°E, the highest brightness temperatures along the equator, indicative of frequent clear skies, were usually found over the open ocean to the north of the land. The level of peak upward motion also ascended from near 700 hPa around 150°E to 350 hPa around 170°E, indicating convective intensification over the warm pool.

Figure 12b shows the east–west variation of IOP-mean SSTs between 5°N and 5°S. The data, based on the global SST analyses from the Coupled Model Project at NMC, were produced weekly on a 1° grid (Reynolds and Smith 1994). Higher SSTs (above 29.3°C) can be observed between 170° and 180°, decreasing toward the west to 28.8°C around 140°E. Comparisons of the vertical heating profiles over the Global Atmospheric Research Program (GARP) Atlantic Tropical Experiment (1974) area and the western Pacific suggest that a higher altitude of heating maximum is usually correlated with higher SSTs (Webster 1991; Webster and Lukas 1992). The zonal variation of SSTs and vertical motion from 140° to 170°E appears to support these findings. A number of studies have suggested that deep convection usually occurs more frequently and more intensively over the areas with higher SSTs up to some threshold, approximately 27.5°–28°C (e.g., Gadgil et al. 1984; Graham and Barnett 1987). How-

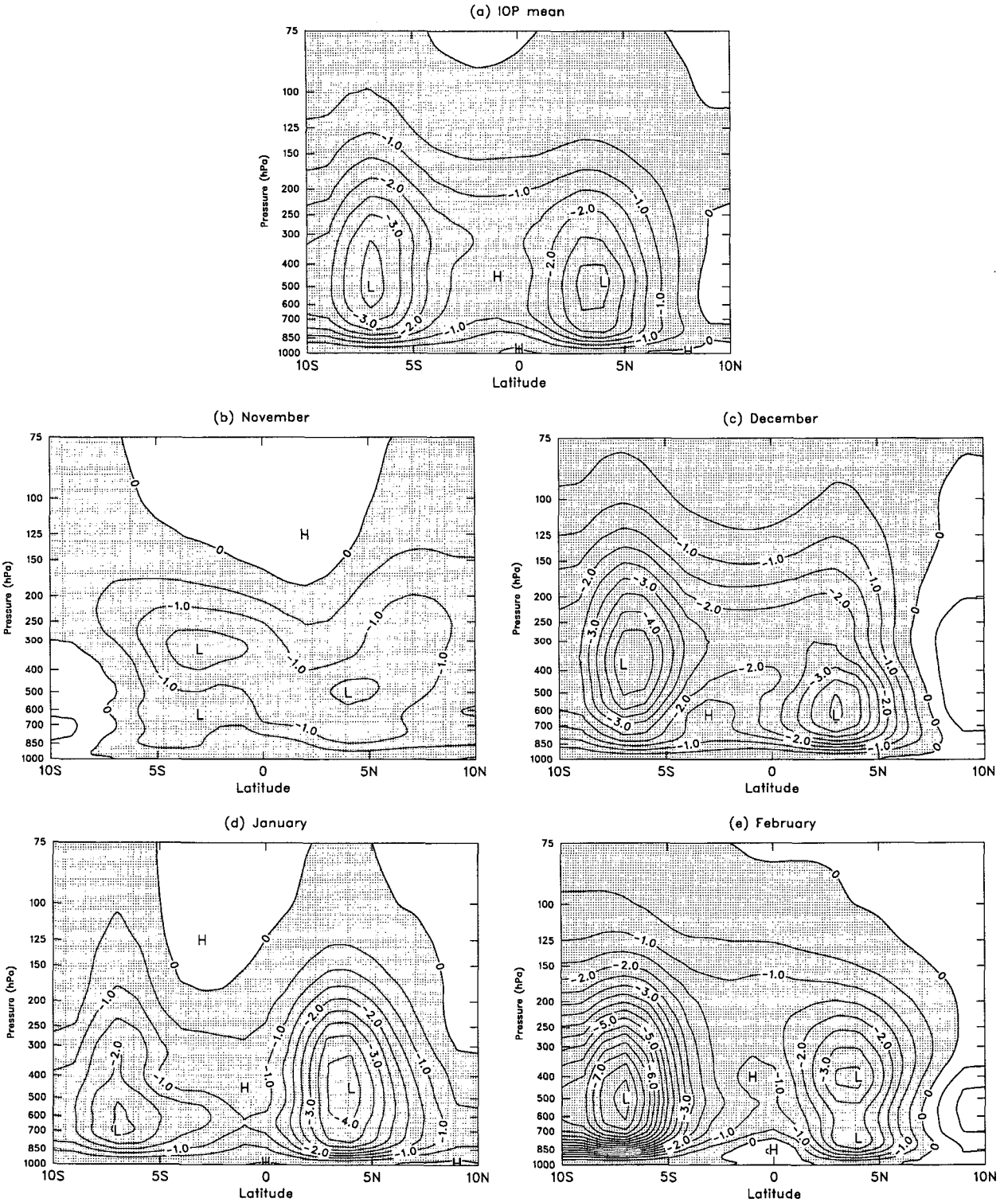

FIG. 11. North–south cross section of ω (mb h^{-1}) between 150° and 160°E. Regions of upward motion are shaded. (a) IOP mean, (b) Nov, (c) Dec, (d) Jan, (e) Feb. Contour interval is 0.5 mb h^{-1}.

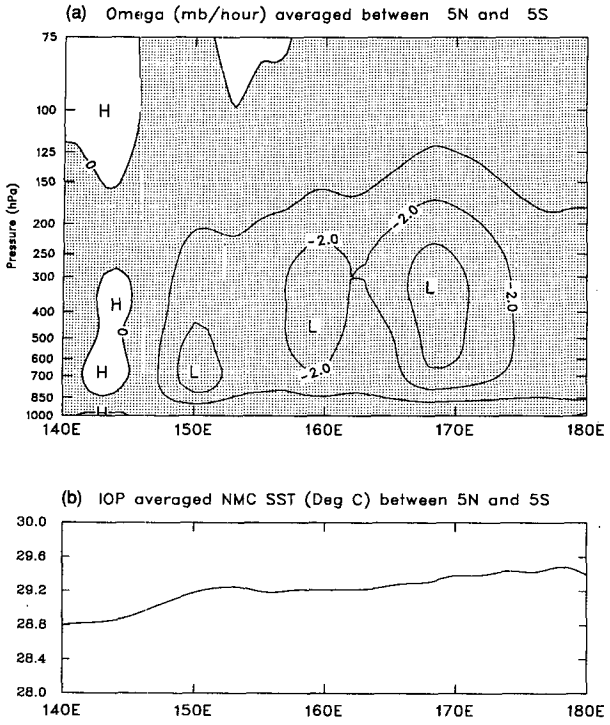

FIG. 12. (a) East–west cross section of IOP-mean ω averaged between 5°N and 5°S. Shaded regions indicate upward motion. (b) East–west variation of NMC SST averaged between 5°N and 5°S (°C).

ever, SST over the COARE LSA always exceeded this threshold, yet a relationship between SST, OLR, and vertical motion continued to exist. From Fig. 12, the intensity of upward motion decreased from 170°E to the date line, although SSTs kept increasing to 29.5°C at 178°E. Waliser et al. (1993) and Waliser and Graham (1993), using satellite data, found that the amount/intensity of convection tends to decrease with increasing SST at temperatures above about 29.5°C. It is possible that the COARE data support this idea; however, the relationship between convection and SST over the warm pool cannot be described in simple terms, rather it is a complex function of evaporation, cloud cover, precipitation, and ocean mixing—all of which are strongly modulated on the timescale of the 30–60-day oscillation (Webster 1994).

5. Basic thermodynamic features

a. Humidity

Figure 13 shows the time series of the IFA-mean relative humidity profiles and 700-hPa wind speed through the COARE IOP. The RH was calculated with respect to ice above the −10°C level (about 450 hPa) and with respect to liquid water below. Consistent with the vertical motion profiles (Fig. 9b), high RH, suggesting strong upward motion, was observed extending from low to upper levels several weeks prior to the late December westerly wind burst. Dry conditions dominated above about 800 hPa when the peak westerly winds prevailed. At this time, peak RH was usually located at low levels between 900 and 950 hPa or near the top of the mixed layer; however, a secondary peak in late December was observed at middle to upper levels where there was strong upward motion (Fig. 9b). Strong advection of dry air in the middle and low levels can often be observed during the COARE IOP (e.g., Numaguti et al. 1995; Mapes and Zuidema 1996). These dry intrusions emanated from the subtropics of both hemispheres and may account for some of the dry episodes in Fig. 13.

Figure 14 shows the IOP-mean relative humidity profiles over the IFA. Two solid curves were generated from COARE data: one with respect to liquid water and the other with respect to ice above the 0°C level. ECMWF and NMC operational analyses are used for comparisons with the COARE sounding data. ECMWF data are at 12 vertical levels, while NMC data are at 11 (standard mandatory) levels. The horizontal resolution of both model analyses is 2.5 degrees, which is converted to 1.0 degree in order to match the sounding analysis.

Both ECMWF model-assimilated and rawinsonde results show a primary peak at low levels at the top of

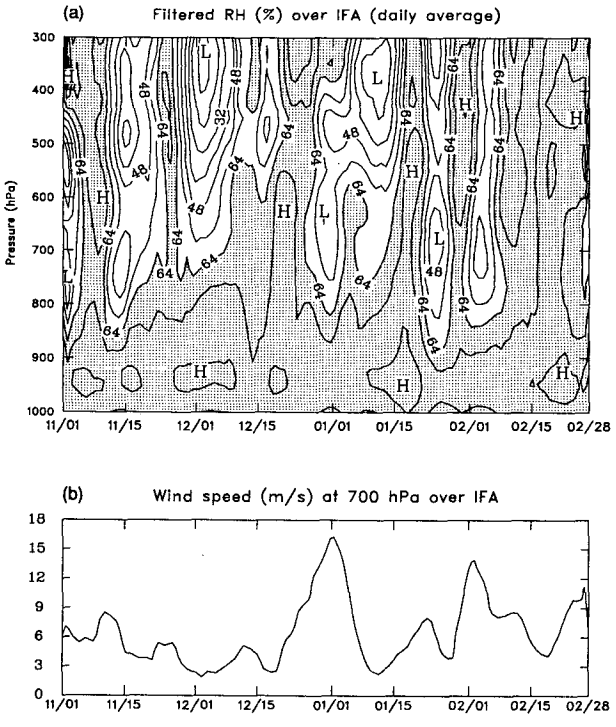

FIG. 13. (a) Time series of the daily mean relative humidity (%) over the Intensive Flux Array. Shaded area indicates RH > 64%. (b) Time series of the IFA-mean wind speed (m s^{-1}) at 700 hPa (5-day running mean).

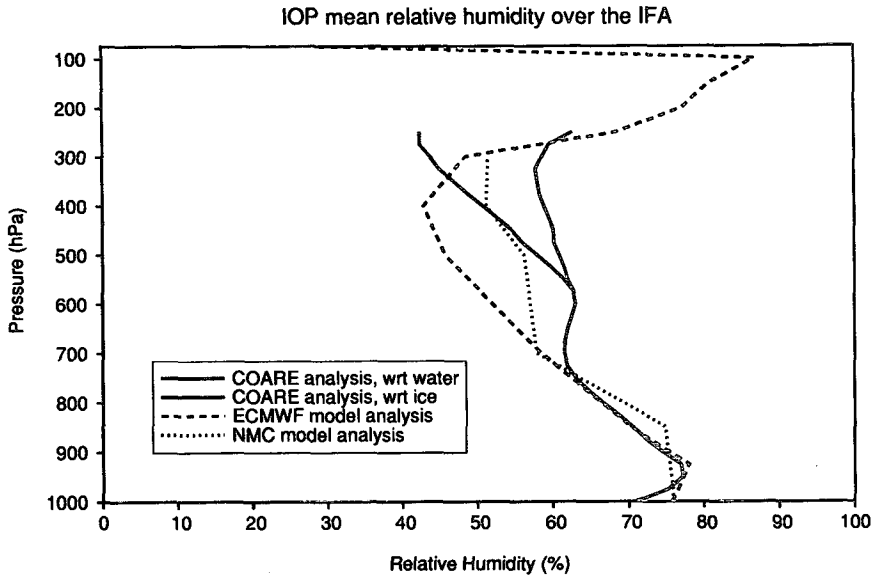

FIG. 14. IOP-mean profiles of relative humidity over the IFA. Solid lines are from the COARE analysis, with respect to liquid water and ice. Dashed lines are from ECMWF and NMC model assimilated analyses.

the mixed layer (~950 hPa), consistent with previous studies of tropical humidity profiles (Liu et al. 1991; Gutzler 1993). They agree very well between 750 and 925 hPa, with a linear relationship between pressure and RH. The NMC model-assimilated profile, however, shows the maximum RH near the surface, decreasing gradually from 1000 to 850 hPa, probably due to coarser vertical resolution (ECMWF data have an extra level at 925 hPa). The primary peak at the top of the mixed layer is not captured.

The biggest discrepancy among the COARE data and model analyses occurs at middle levels. The COARE mean RH gradually increases above 700 hPa and shows an apparent secondary peak near 550 hPa (near the 0°C level). This feature has not received much attention, although it can be noticed in the climatological studies of Oort (1983), Liu et al. (1991), and Gutzler (1993). Ciesielski et al. (1995) have recently investigated this feature and related it to stable layers near the 0°C level associated with melting in precipitating systems. They argued that deep convection penetrating or congestus impinging upon the stable layers could lead to enhanced detrainment and moistening near that level. Another possibility is that a significant number of mesoscale convective systems with attendant saturated upper-tropospheric stratiform regions could perturb the mean RH profile in the manner shown in Fig. 14. The secondary peak, however, is not present in either ECMWF or NMC operational analyses (although it is more closely matched by NMC). The midtroposphere is much drier in the two model analyses, particularly in the ECMWF model as also noted by Schmetz and Van den Berg (1994). In the upper troposphere, the ECMWF RH increases rapidly and shows a peak at about 100 hPa, presumably due to cirrus clouds associated with deep convection. Although RH sampling is questionable above 250 hPa, the COARE analysis with respect to ice also shows an increasing tendency above 300 hPa.

b. Temperature perturbations

Time series of daily averaged temperature perturbations and brightness temperature (repeated from Fig. 9a) over the IFA are illustrated in Fig. 15. Two warm anomalies, possibly associated with latent heat release (Reed and Recker 1971)—longwave radiative warming (Webster and Stephens 1980) or shortwave absorption (Randall et al. 1991)—can be clearly seen in the middle and upper troposphere (Fig. 15a) during the active phases of the 30–60 day oscillation (e.g., 5–25 December, 13–22 January), when upward motion was the strongest (Fig. 9) and high cloud coverage was a maximum (Fig. 15b). This feature is consistent with the easterly wave composite findings in Reed and Recker (1971) and Thompson et al. (1979), although their composited temperature anomalies were smaller. Anomalous cooling can be seen at low levels during these active phases, possibly due to melting and evaporation in downdrafts (Zipser 1969; Reed and Recker 1971) or as a large-scale response to upper-level heating (e.g., Mapes and Houze 1995). Strong anomalous cooling, presumably induced by overshooting cumulonimbus tops and/or longwave cooling (Webster and Stephens 1980), existed near and above the tropopause around 100 hPa (between 5 and 24 December and 16

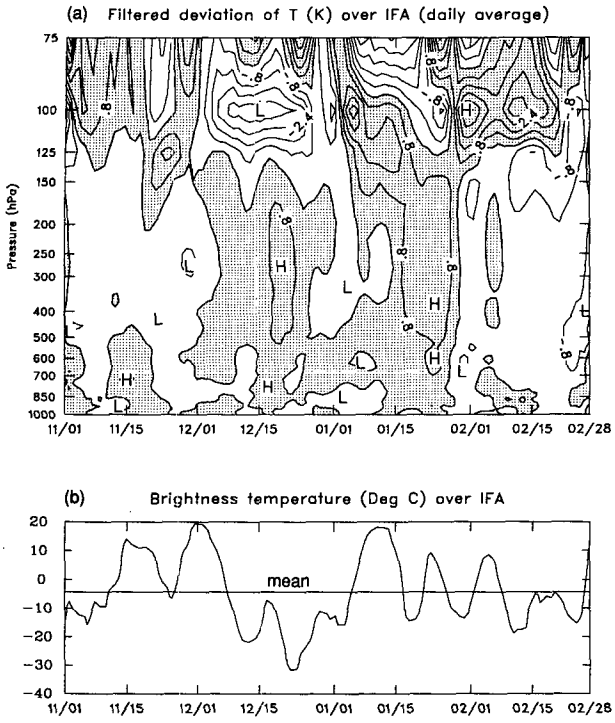

FIG. 15. (a) Time series of temperature perturbation (deviation from the COARE mean) over the IFA. Contour interval 0.8 K, and anomalous warming is shaded. (b) Time series of the IFA-averaged GMS brightness temperature (°C).

and 20 January), very similar to those shown in Reed and Recker (1971) and Thompson et al. (1979). Johnson and Kriete (1982) observed similar strong cooling above mesoscale convective systems just north of Borneo during December 1979. Hendon and Liebmann (1990b) showed a temperature perturbation plot (their Fig. 5d) for a composited 30–60 day oscillation. The rainfall region in their study also coincided well with a warm middle and upper troposphere and a cool pool below 850 hPa. However, the anomalous cooling feature near 100 hPa is not present in their analysis. During the period when the low-level westerlies were strong, cool anomalies generally dominated the middle and upper troposphere (Fig. 15a).

6. Synthesis of observations

Madden and Julian (1972), in a broad-scale sense, schematically depicted the 30–60 day oscillation as a large-scale disturbance originating over the Indian Ocean and propagating into the tropical Pacific. Lau et al. (1989), based mainly on satellite observations and numerical model results, schematically showed the mutual connection among super cloud cluster (Nakazawa 1988), westerly wind bursts, and the 30–60 day oscillations in the western Pacific (see their Fig. 13). In this paper, the observed characteristics of the December–early January westerly wind burst, the most prominent in COARE, are synthesized (Fig. 16) based on the kinematic and thermodynamic features over the IFA from rawinsonde analyses and ISS surface and buoy data. The data are presented with time increasing to the left so that the section can also be thought of as an east–west section (west on left); however, the extent to which a time to space transformation can be made is limited since analysis of preliminary data from over Indonesia suggests that much of the intensification of the low-level westerlies and upper-level easterlies occurs in situ and cannot be completely explained by propagation from the west. In this composite, day 0 corresponds to 1 January.

About 4–6 weeks prior to the peak westerly wind burst (day −37.5), convection was generally suppressed over the western Pacific warm pool. Weak winds dominated through the entire troposphere, and the vertical wind shear was very weak. The SST was at its maximum during this suppressed phase, and both surface sensible and latent heat fluxes were relatively small.

About 10 days after the suppressed period (day −25), convection gradually intensified over the warm pool. Westward propagating convective systems, usually with 2-day life cycles (Sui and Lau 1992; Hendon and Liebmann 1994; Takayabu 1994), were observed near the equator. The zonal winds were dominated by easterlies above about 900 hPa with a peak near 100 hPa. Weak westerlies appeared near the surface, and the convective intensity was likely enhanced by the convergence between westerlies and weak easterlies at low levels. Moistening occurred through most of the troposphere, and warm anomalies can be observed at the middle and upper troposphere. Cool anomalies usually occurred near the surface and the tropopause.

One to two weeks prior to the peak westerly wind burst (day −12.5), vigorous convection continued to occur over the warm pool, although it was episodic with frequent westward propagating systems. However, the large-scale envelope of convection propagated eastward. The most prominent feature during this stage was the rapid increase of the midtropospheric vertical wind shear within the convective systems: strengthening westerlies can be observed at middle and low levels (with a peak around 800 hPa) and strong easterlies aloft. The thermodynamic features within the convective systems are similar to those at day −25. In addition, the areal coverage of anvil clouds and high cirrus increased during the latter part of this stage. In an average sense, the surface wind speed gradually increased with time, and SSTs continued to drop, in association with increased evaporative cooling, cloud cover, and ocean mixing (Chu and Frederick 1990; Webster 1994). Superimposed on the large-scale evolution are short-period features induced by the convective systems. Stronger surface wind speeds along with peaks in the surface latent and sensible heat fluxes can be

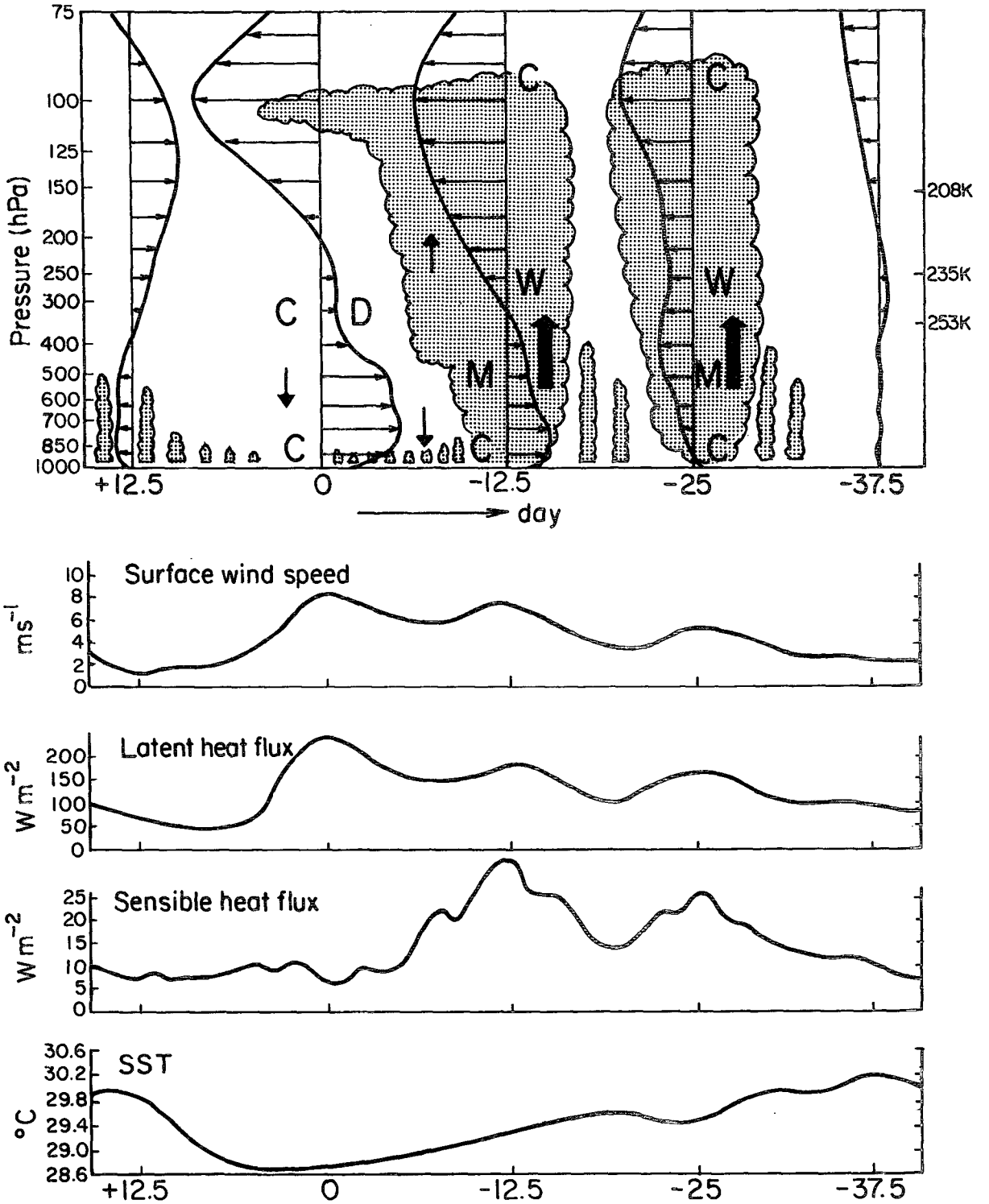

FIG. 16. A descriptive model of the kinematic, thermodynamic, and surface properties of the December to early January westerly wind burst as it passed the IFA. Day 0 is time of maximum low-level westerlies, with earlier times indicated by negative days (placed to the right so that the left portion of the diagram is to the west: see caution in text, however, about fully interpreting diagram as west–east section). Letters in figure refer to anomalies W: warm, C: cool, M: moist, and D: dry. Heavy arrows indicate strong vertical motion; light arrows weak vertical motion. Clouds are schematic, horizontal scales exaggerated. Temperatures corresponding to pressure levels are indicated on right.

observed with the passage of the major convective systems (see Fig. 9b).

At the time of the peak westerly wind burst (day 0), downward motion generally dominated the middle and low levels, and convection was typically suppressed. Tropospheric vertical wind shear was strongest during this stage with deep westerlies underlying strong upper-level easterlies. Cool anomalies occurred in the upper troposphere and at low levels. Surface wind speeds reached their maxima, while SSTs continued to decrease until several days after the passage of the peak westerly wind burst. It is interesting to note that, while surface latent heat fluxes followed the surface wind speed and showed a primary peak at this stage, sensible heat fluxes peaked at an earlier time. The absence of a peak in the sensible heat flux at time 0 is related to the strong cooling of the ocean surface at the time of maximum mixing.

About 1–2 weeks after the passage of the peak westerly wind burst (day +12.5), surface wind speeds fell to 2–3 m s^{-1}, and the SST gradually recovered. Weak easterlies appeared at middle and low levels, and numerous shallow clouds were observed over the warm pool. Vertical wind shears became much, weaker and both surface latent and sensible heat fluxes returned to near their mean values (116 W m^{-2} and 11 W m^{-2}, respectively).

7. Summary and discussion

Rawinsonde and GMS IR data have been used to document the mean and transient behavior and horizontal convective variability of the atmosphere over the warm pool throughout the 4-mo TOGA COARE IOP. IOP-mean brightness temperatures indicate that the maximum deep convection was located in the eastern part of the LSA between 170°E and 180°, similar to the findings of Gutzler et al. (1994). The IFA was in a transition zone with a minimum in deep convection to the west. Cold clouds were usually found over large islands such as New Guinea, and a double-ITCZ structure was usually observed along the equator north and south of the IFA. Although there was a general north to south shift in convection during the IOP, marked variability in the patterns occurred on a month-to-month basis.

Three prominent westerly wind burst episodes passed the COARE domain during the IOP: early to middle November, middle December to early January, and late January to the end of February. In the major event between December and January, maximum easterlies of 37 m s^{-1} in the upper troposphere and maximum westerlies of 17 m s^{-1} at low levels averaged over the IFA occurred at the time of the peak wind burst. During this event, westerly winds dominated most of the troposphere and extended from the surface to 200 hPa, possibly influenced by Tropical Cyclones Kina and Nina. The out-of-phase relationship between upper-level and low-level winds is consistent with previous findings (Madden and Julian 1971, 1972; Knutson and Weickmann 1987), although the vertical wind shear measured during COARE was far greater than previously recognized.

Infrared and 1000-hPa zonal wind data indicate that both the December–January and the February westerly wind bursts occurred south of 3°N, with their westerly maxima centered near 5°S. There was a general absence of mean equatorial easterlies south of 3°N during the COARE IOP when these westerly wind bursts occurred. Low-level westerly winds following the disturbance associated with the 30–60 day oscillation were always stronger than the winds preceding it. This evidence does not appear to support the WISHE mechanism (Emanuel 1987; Neelin et al. 1987), which requires a preexisting tropical mean easterly and stronger perturbation winds to the east of the disturbance to explain the maintenance and eastward propagation of the 30–60 day oscillation. Further evidence from the IMET buoy and ISS surface data indicates that the maximum surface energy transfer usually occurred during and after the arrival of the disturbance associated with the 30–60 day oscillation.

The IOP-mean divergence profiles within the double ITCZ show strong low-level convergence from the surface to about 700 hPa with strong divergence above 300 hPa, consistent with previous studies in the tropical western Pacific (Reed and Recker 1971; Yanai et al. 1973). The IFA was located between the double-ITCZ bands with weak convergence at middle and low levels and divergence aloft. Averaged over the entire IOP, maximum convergence in the IFA was located between 700 and 800 hPa with very weak divergence near the surface; however, IFA profiles at times of deep convection closely resembled those in the ITCZ bands to the north and south. Therefore, although the divergence and vertical motion profiles tend to look alike whenever and wherever the convection is strong, caution should be exercised in generalizing long-period mean divergence and vertical motion profiles from one region to another over the western Pacific warm pool.

A double-ITCZ structure can be clearly observed in both vertical motion and divergence cross sections across the equator. While there was upward motion in the mean over the warm pool during the COARE IOP, the strong upward motion over the IFA, indicative of enhanced convection, usually occurred 1–3 weeks prior to the peak westerly wind burst, with peak upward motion located at upper levels between 500 and 350 hPa. Subsidence or weak upward motion was observed when the peak westerly winds prevailed. The IOP-averaged vertical motion shows apparent zonal variations along the equator in the LSA, with the climatological mean center of deep convection around 170°E, consistent with brightness temperature data. The magnitudes of upward motion gradually increased with SST from the west to the east, and the altitude of the peak also

increased from low levels in the western part of LSA to upper levels around 170°E.

Very cold clouds were found to be a good indicator of vertical motion only at upper levels. At low levels (IFA-mean brightness temperatures above −20°C or cloud tops below 375 hPa), vertical motion at 700 hPa was essentially independent of cloud-top temperature. For IFA-mean brightness temperatures below −20°C, about one-third of the cases show downward motion at 700 hPa, suggesting a significant number of cases in which deep convection was absent under very cold cloud tops or mesoscale downdrafts below stratiform precipitation anvils were occurring (Houze 1982). Extensive optically thick anvil cloud and nonprecipitating high cirrus are believed to dominate the IFA in these cases.

The IOP-averaged relative humidity profile over the IFA shows a primary peak at low levels at the top of the mixed layer (~950 hPa). A secondary peak can be clearly seen around 550 hPa (near the 0°C level), which has been related to stable layers near the 0°C level associated with melting in precipitating systems (Ciesielski et al. 1995). The secondary peak at middle levels is not present in either ECMWF or NCEP operational model-assimilated analyses, possibly due in part to coarser resolution in the models.

Based on the kinematic and thermodynamic features in the atmosphere, and surface and buoy data, a descriptive model is constructed to illustrate the life cycle of the December–January COARE westerly wind burst. This model is not intended to apply to all westerly wind bursts in the equatorial Pacific. The vertical wind shear gradually increases as the peak westerly wind bursts approaches, and SST continues to drop with strengthening surface wind speed. Surface sensible heat flux peaks prior to the strongest westerlies, while the latent heat flux peaks at the time of the peak westerly winds.

The results of this study will be extended in a forthcoming paper that will describe the vertical and horizontal distributions of heating and moistening over the warm pool. Surface rainfall rates and radiative effects will be estimated from budget determinations.

Acknowledgments. The authors would like to thank our colleagues Paul Ciesielski, Jim Bresch, Rick Taft, and Bill Gallus for their help with the COARE data management and processing. Dr. Steve Lord at NCEP kindly provided a cubic-spline analysis package for comparison of objective analysis schemes. Corrected COARE rawinsonde data from the ISS systems were provided to us by Erik Miller (NCAR/SSSF) and from COARE priority stations by Jim Moore (NCAR/OFPS). Japanese GMS satellite data were provided to us by Dr. Tetsuo Nakazawa. Thanks also go to Drs. Bob Weller and Steve Anderson for providing the IMET buoy data (including surface heat fluxes) and to Drs. Frank Bradley and Chris Fairall for providing the code to compute surface heat fluxes. Professor David Randall and Paul Ciesielski made helpful comments and suggestions in the early version of the paper. Constructive comments from Prof. David Gutzler and two anonymous reviewers greatly improved the original manuscript. Special appreciation is extended to Profs. Roger Lukas and Peter Webster for their exceptional efforts in conceiving, planning, and implementing TOGA COARE.

This research has been supported by a NASA Graduate Fellowship on Global Change under Grant NGT-30190 and by the National Oceanic and Atmospheric Administration under Grants NA90RAH00077 and NA37RJ0202.

REFERENCES

Arkin, P. A., and B. N. Meisner, 1987: The relationship between large-scale convective rainfall and cold cloud over the western hemisphere during 1982–84. *Mon. Wea. Rev.*, **115**, 51–74.

Barnes, S. L., 1964: A technique for maximizing details in numerical weather map analysis. *J. Appl. Meteor.*, **3**, 396–409.

——, 1973: Mesoscale objective map analysis using weighted time-series observations. NOAA Tech. Memo. ERL NSSL-62, Norman, OK, 60 pp.

Bellamy, J. C., 1949: Objective calculations of divergence, vertical velocity, and vorticity. *Bull. Amer. Meteor. Soc.*, **30**, 45–49.

Chang, C.-P., 1977: Viscous internal gravity waves and low-frequency oscillations in the tropics. *J. Atmos. Sci.*, **34**, 901–910.

——, and K.-M. Lau, 1980: Northeasterly cold surges and near-equatorial disturbances over the winter MONEX area during December 1994. Part II: Planetary-scale aspects. *Mon. Wea. Rev.*, **108**, 298–312.

——, and ——, 1982: Short-term planetary-scale interactions over the tropics and midlatitudes during northern winter. Part I: Contrasts between active and inactive periods. *Mon. Wea. Rev.*, **110**, 933–946.

——, and H. Lim, 1988: Kelvin wave-CISK: A possible mechanism for the 30–50 day oscillation. *J. Atmos. Sci.*, **45**, 1709–1720.

Chao, W. C., and S.-J. Lin, 1994: Tropical intraseasonal oscillation, super cloud clusters, and cumulus convective schemes. *J. Atmos. Sci.*, **51**, 1282–1297.

Chu, P.-S., 1988: Extratropical forcing and the burst of equatorial westerlies in the western Pacific: A synoptic study. *J. Meteor. Soc. Japan*, **66**, 549–564.

——, and J. Frederick, 1990: Westerly wind bursts and surface heat fluxes in the equatorial western Pacific in May 1982. *J. Meteor. Soc. Japan*, **68**, 523–537.

Ciesielski, P. E., R. H. Johnson, and K. A. Hart, 1995: Temperature and moisture inversions near the 0°C level in TOGA COARE. Preprints, *21st Conf. on Hurricane and Tropical Meteorology*, Miami, FL, Amer. Meteor. Soc., 547–549.

Davies-Jones, R. P., 1993: Useful formulas for computing divergence, vorticity, and their errors from three or more stations. *Mon. Wea. Rev.*, **121**, 713–725.

Emanuel, K. A., 1987: An air–sea interaction model of intraseasonal oscillations in the tropics. *J. Atmos. Sci.*, **44**, 2324–2340.

——, 1988: Reply. *J. Atmos. Sci.*, **45**, 3528–3530.

——, J. D. Neelin, and C. S. Bretherton, 1994: On the large-scale circulation of the convecting atmospheres. *Quart. J. Roy. Meteor. Soc.*, **120**, 1111–1143.

Fairall, C. W., E. F. Bradley, D. P. Rogers, J. B. Edson, and G. S. Young, 1995: Bulk parameterization of air–sea fluxes for TOGA COARE. *J. Geophys. Res.*, in press.

Gadgil, S., P. V. Joseph, and N. V. Joshi, 1984: Ocean–atmosphere coupling over monsoon regions. *Nature*, **312**, 141–143.

Gill, A., 1980: Some simple solutions for heat induced tropical circulations. *Quart. J. Roy. Meteor. Soc.*, **106**, 447–462.

Graham, N. E., and T. P. Barnett, 1987: Sea surface temperature, surface wind divergence and convection over tropical oceans. *Science,* **238,** 657–659.

Gray, W. M., 1979: Hurricanes: Their formation, structure and likely role in the tropical circulation. *Meteorology over the Tropical Oceans,* D. B. Shaw, Ed., Royal Meteorology Society, 156–218.

Gutzler, D. S., 1991: Interannual fluctuations of intraseasonal variance of near-equatorial zonal winds. *J. Geophys. Res.,* **96**(suppl), 3172–3185.

——, 1993: Uncertainties in climatological tropical humidity profiles: Some implications for estimating the greenhouse effect. *J. Climate,* **6,** 978–982.

——, G. N. Kiladis, G. A. Meehl, K. M. Weickmann, and M. Wheeler, 1994: Seasonal climate summary: The global climate of December 1992–February 1993. Part II: Large-scale variability across the tropical western Pacific during TOGA COARE. *J. Climate,* **7,** 1606–1622.

Harrison, D. E., and P. S. Schopf, 1984: Kelvin-wave-induced anomalous advection and the onset of surface warming in El Niño events. *Mon. Wea. Rev.,* **112,** 923–933.

Hayashi, Y., and D. G. Golder, 1993: Tropical 40–50- and 25–30-day oscillations appearing in realistic and idealized GFDL climate models and the ECMWF dataset. *J. Atmos. Sci.,* **50,** 464–494.

Hendon, H. H., and B. Liebmann, 1990a: A composite study of onset of the Australian summer monsoon. *J. Atmos. Sci.,* **47,** 2227–2240.

——, and ——, 1990b: The intraseasonal (30–50 day) oscillation of the Australian summer monsoon. *J. Atmos. Sci.,* **47,** 2909–2923.

——, and ——, 1994: Organization of convection within the Madden–Julian oscillation. *J. Geophys. Res.,* **99,** 8073–8083.

Holland, G. J., 1986: Interannual variability of the Australian summer monsoon at Darwin: 1952–82. *Mon. Wea. Rev.,* **114,** 594–604.

Houze, R. A., Jr., 1982: Cloud clusters and large-scale vertical motions in the tropics. *J. Meteor. Soc. Japan,* **60,** 396–409.

Hu, Q., and D. A. Randall, 1994: Low-frequency oscillations in radiative–convective systems. *J. Atmos. Sci.,* **51,** 1089–1099.

Johnson, R. H., and D. C. Kriete, 1982: Thermodynamic and circulation characteristics of winter monsoon tropical mesoscale convection. *Mon. Wea. Rev.,* **110,** 1898–1911.

Keen, R. A., 1982: The role of cross-equatorial tropical cyclone pairs in the Southern Oscillation. *Mon. Wea. Rev.,* **110,** 1405–1416.

——, 1988: Equatorial westerlies and southern oscillation. *Proc. of the US TOGA Western Pacific Air–Sea Interaction Workshop,* R. Lukas and P. Webster Eds., U.S. TOGA Rep. USTOGA-8, University Corp. of Atmos. Res., 121–140.

Kiladis, G. N., G. A. Meehl, and K. M. Weickmann, 1994: Large-scale circulation associated with westerly wind bursts and deep convection over the western equatorial Pacific. *J. Geophys. Res.,* **99,** 18 527–18 544.

Knutson, T. R., and K. M. Weickmann, 1987: 30–60 day atmospheric oscillations: Composite life cycles of convection and circulation anomalies. *Mon. Wea. Rev.,* **115,** 1407–1436.

Krishnamurti, T. N., and D. Subrahmanyam, 1982: The 30–50 day mode at 850 mb during MONEX. *J. Atmos. Sci.,* **39,** 2088–2095.

Lander, M. A., 1990: Evolution of the cloud pattern during the formation of tropical cyclone twins symmetrical with respect to the equator. *Mon. Wea. Rev.,* **118,** 1194–1202.

Lau, K.-M., and P. H. Chan, 1986: The 40–50 day oscillation and the El Niño/Southern Oscillation. A new perspective. *Bull. Amer. Meteor. Soc.,* **67,** 533–534.

——, and L. Peng, 1987: Origin of low-frequency (intraseasonal) oscillations in the tropical atmosphere. Part I: Basic theory. *J. Atmos. Sci.,* **44,** 950–972.

——, and P. H. Chan, 1988: Interannual and intraseasonal variations of tropical convection: A possible link between the 40-day mode and ENSO. *J. Atmos. Sci.,* **45,** 506–521.

——, C.-P. Chang, and P. H. Chan, 1983: Short-term planetary-scale interactions over the tropics and midlatitudes. Part II: Winter MONEX period. *Mon. Wea. Rev.,* **111,** 1372–1388.

——, L. Peng, C.-H. Sui, and T. Nakazawa, 1989: Dynamics of supper cloud clusters, westerly wind burst, 30–60 day oscillation and ENSO: An unified view. *J. Meteor. Soc. Japan,* **67,** 205–219.

Lau, N.-C., 1985: Modeling the seasonal dependence of the atmospheric response to observed El Niños in 1962–76. *Mon. Wea. Rev.,* **113,** 1970–1976.

Lin, X., and R. H. Johnson, 1994: Preliminary heat and moisture budgets and thermodynamic features over TOGA COARE region. Preprints, *Sixth Conf. on Mesoscale Processes.* Portland, OR, Amer. Meteor. Soc., 17–20.

Liu, W. T., K. B. Katsaros, and J. A. Businger, 1979: Bulk parameterization of air–sea exchanges of heat and water vapor including the molecular constraints at the interface. *J. Atmos. Sci.,* **36,** 1722–1735.

——, W. Tang, and P. P. Niller, 1991: Humidity profiles over the ocean. *J. Climate,* **4,** 1023–1034.

Love, G., 1985: Cross-equatorial influence of winter hemisphere subtropical cold surges. *Mon. Wea. Rev.,* **113,** 1487–1498.

Luther, D. S., D. E. Harrison, and R. A. Knox, 1983: Zonal winds in the central equatorial Pacific and El Niño. *Science,* **222,** 327–330.

Madden, R. A., and P. R. Julian, 1971: Description of a 40–50 day oscillation in the zonal wind in the tropical Pacific. *J. Atmos. Sci.,* **28,** 702–708.

——, and ——, 1972: Description of global-scale circulation cells in the tropics with a 40–50 day period. *J. Atmos. Sci.,* **29,** 1109–1123.

——, and ——, 1994: Observations of the 40–50-day tropical oscillation—A review. *Mon. Wea. Rev.,* **122,** 814–837.

Magaña, V., and M. Yanai, 1991: Tropical–midlatitude interaction on the time scale of 30 to 60 days during the northern summer of 1979. *J. Climate,* **4,** 180–201.

Mapes, B. E., and R. A. Houze Jr., 1995: Diabatic divergence profiles in western Pacific mesoscale convective systems. *J. Atmos. Sci.,* **52,** 1807–1828.

——, and P. Zuidema, 1996: Radiative-dynamical consequences of dry tongues in the tropical troposphere. *J. Atmos. Sci.,* **53,** 620–638.

McBride, J. L., N. E. Davidson, K. Puri, and G. C. Tyrell, 1995: The flow during TOGA COARE as diagnosed by the BMRC tropical analysis and prediction system. *Mon. Wea. Rev.,* **123,** 717–736.

Nakazawa, T., 1988: Tropical super cluster within intraseasonal variations over the western Pacific. *J. Meteor. Soc. Japan,* **66,** 823–839.

Neelin, J. D., I. M. Held, and K. H. Cook, 1987: Evaporation–wind feedback and low-frequency variability in the tropical atmosphere. *J. Atmos. Sci.,* **44,** 2341–2348.

Nitta, T., 1972: Energy budget of wave disturbance over the Marshall Islands during the years of 1956 and 1958. *J. Meteor. Soc. Japan,* **50,** 71–84.

——, 1989: Development of a twin cyclone and westerly bursts during the initial phase of the 1986–87 El Niño. *J. Meteor. Soc. Japan,* **67,** 677–681.

——, and T. Motoki, 1987: Abrupt enhancement of convective activity and low-level westerly wind burst during the onset phase of 1986–87 El Niño. *J. Meteor. Soc. Japan,* **65,** 497–506.

Numaguti, A., R. Oki, K. Nakamura, K. Tsuboki, N. Misawa, T. Asai, and Y.-M. Kodama, 1995: 4-5-day-period variation and low-level dry air observed in the equatorial western Pacific during the TOGA-COARE IOP. *J. Meteor. Soc. Japan,* **73,** 267–290.

Ogura, Y., and H.-N. Chin, 1987: A case study of cross-equatorial twin vortices over the Pacific in the northern winter using FGGE data. *J. Meteor. Soc. Japan,* **65,** 669–674.

Oort, A. H., 1983: Global atmospheric circulations statistics, 1958–73. NOAA Prof. Paper 14., 180 pp.

Ooyama, K. V., 1987: Scale-controlled objective analysis. *Mon. Wea. Rev.,* **115,** 2479–2506.

Parker, D. E., 1973: Equatorial Kelvin waves at 100 millibars. *Quart. J. Roy. Meteor. Soc.*, **99**, 116–129.

Parsons, D., W. Dabberdt, H. Cole, T. Hock, C. Martin, A.-L. Barrett, E. Miller, M. Spowart, M. Howard, W. Ecklund, D. Carter, K. Gage, and J. Wilson, 1994: The Integrated Sounding System: Description and preliminary observations from TOGA COARE. *Bull. Amer. Meteor. Soc.*, **75**, 553–567.

Peixoto, J. P., and A. H. Oort, 1992: *Physics of Climate.* American Institute of Physics, 520 pp.

Randall, D. A., Harshvardhan, and D. A. Dazlich, 1991: Diurnal variability of the hydrologic cycle in a general circulation model. *J. Atmos. Sci.*, **48**, 40–62.

Reed, R. J., and E. E. Recker, 1971: Structure and properties of synoptic-scale wave disturbances in the equatorial western Pacific. *J. Atmos. Sci.*, **28**, 1117–1133.

Reynolds, R. W., and T. S. Smith, 1994: Improved global sea surface temperature analyses using optimum interpolation. *J. Climate*, **7**, 929–948.

Riehl, H., 1954: *Tropical Meteorology.* McGraw-Hill, 392 pp.

——, and J. S. Malkus, 1958: On the heat balance in the equatorial trough zone. *Geophysica*, **6**, 503–538.

Schmetz, J., and L. Van den Berg, 1994: Upper tropospheric humidity observations from Meteosat compared with short term forecast fields. *Geophys. Res. Lett.*, **21**, 573–576.

Sui, C.-H., and K.-M. Lau, 1992: Multiscale phenomena in the tropical atmosphere over the western Pacific. *Mon. Wea. Rev.*, **120**, 407–430.

Takayabu, Y. N., 1994: Large-scale cloud disturbances associated with equatorial waves. Part II: Westward-propagating inertio gravity waves. *J. Meteor. Soc. Japan*, **72**, 451–465.

Thompson, R. M., Jr., S. W. Payne, E. E. Recker, and R. J. Reed, 1979: Structure and properties of synoptic-scale wave disturbances in the Intertropical Convergence Zone of the eastern Atlantic. *J. Atmos. Sci.*, **36**, 53–72.

Velden, C. S., and J. A. Young, 1994: Satellite observations during TOGA COARE: Large-scale descriptive overview. *Mon. Wea. Rev.*, **122**, 2426–2441.

Waliser, D. E., and N. S. Graham, 1993: Convective cloud systems and warm-pool sea surface temperatures: Coupled interactions and self-regulation. *J. Geophys. Res.* **98**, 12 881–12 893.

——, ——, and C. Gautier, 1993: Comparison of the highly reflective cloud and outgoing longwave datasets for use in estimating tropical deep convection. *J. Climate*, **6**, 331–353.

Wallace, J. M., and V. E. Kousky, 1968: Observational evidence of Kelvin waves in the tropical stratosphere. *J. Atmos. Sci.*, **25**, 900–907.

Wang, B., 1988: Dynamics of tropical low-frequency waves: an analysis of the moist Kelvin wave. *J. Atmos. Sci.*, **45**, 2051–2065.

Webster, P. J., 1991: Ocean–atmosphere interaction in the tropics. ECMWF Seminar Series: Interaction of the mid-latitudes and the tropics. European Centre of Medium-Range Weather Forecasts, Reading, U.K., 67–116.

——, 1994: The role of hydrological processes in ocean–atmosphere interactions. *Rev. Geophys.*, **32**, 427–476.

——, and G. L. Stephens, 1980: Tropical upper-tropospheric extended clouds—Inference from winter MONEX. *J. Atmos. Sci.*, **37**, 1521–1541.

——, and R. Lukas, 1992: TOGA COARE: The Coupled Ocean–Atmosphere Response Experiment. *Bull. Amer. Meteor. Soc.*, **73**, 1377–1416.

Weisman, M. L., J. B. Klemp, and R. Rotunno, 1988: Structure and evolution of numerically simulated squall lines. *J. Atmos. Sci.*, **45**, 1990–2013.

Yamagata, T., and Y. Hayashi, 1984: A simple diagnostic model for the 30–50 day oscillation in the tropics. *J. Meteor. Soc. Japan*, **62**, 709–717.

Yanai, M., S. Esbensen, and J. H. Chu, 1973: Determination of bulk properties of tropical cloud clusters from large-scale heat and moisture budgets. *J. Atmos. Sci.*, **30**, 611–627.

Yano, J. I., and K. A. Emanuel, 1991: An improved model of the equatorial troposphere and its coupling with the stratosphere. *J. Atmos. Sci.*, **48**, 377–389.

Yasunari, T., 1979: Cloudiness fluctuations associated with the Northern Hemisphere summer monsoon. *J. Meteor. Soc. Japan*, **57**, 227–242.

Zipser, E. J., 1969: The role of organized unsaturated convective downdrafts in the structure and rapid decay of an equatorial disturbance. *J. Appl. Meteor.*, **8**, 799–814.